Ramos, M.S.; Farina, L.; Faria, S.H.; Li, C. 2021. **Relationships between large-scale climate modes and the South Atlantic Ocean wave climate.** PROGRESS IN OCEANOGRAPHY. 197. DOI (**10.1016/j.pocean.2021.102660**)

Relationships between large-scale climate modes and the South Atlantic Ocean wave climate

Authors

Marília S. Ramos[1]
[1]Institute of Geosciences, Federal University of Rio Grande do Sul
90650-001 Porto Alegre, RS, Brazil.
E-mail: mariliasr@live.com
Mobile: +5551 99717 2211
ORCID: 0000-0002-8286-4800

Leandro Farina[1,2]
[2]Institute of Mathematics and Statistics, Federal University of Rio Grande do Sul
90650-001, Porto Alegre, RS, Brazil
E-mail: farina@mat.ufrgs.br
ORCID: 0000-0003-2744-515X

Sérgio Henrique Faria[3,4]
[3]Basque Centre for Climate Change (BC3)
48940 Leioa, Spain
[4]IKERBASQUE, Basque Foundation for Science
48011 Bilbao, Spain
E-mail: sh.faria@bc3research.org
ORCID: 0000-0002-8825-7518

Chen Li[5]
[5]ARC Centre of Excellence for Climate Extremes
School of Earth, Atmosphere and Environment
Monash University, VIC 3008, Australia
E-mail: chen.li2@monash.edu
ORCID: 0000-0002-3811-4236

Acknowledgements

MSR would like to thank CAPES for the stipend provided, Professor Léo Hartmann (Federal University of Rio Grande do Sul) for reviewing the manuscript, and Nicolas Bose (Federal University of Rio Grande do Sul) and Joshua Soderholm (Bureau of Meteorology) for all the insights and support. MSR and LF acknowledge support from the project ROAD-BESM – Regional Oceanic and Atmospheric Downscaling/CAPES (88881.146048/2017-01). SHF acknowledges support by the Spanish Government through the María de Maeztu excellence accreditation 2018–2022 (MDM-2017-0714).

Abstract

Modes of variability in ocean wave conditions are coupled to atmospheric circulation changes due to exchange of energy and momentum at the interface. Here, we explored for the South Atlantic Ocean the relations between three main climate oscillations (El Niño–Southern Oscillation [ENSO], Southern Annular Mode [SAM], and Pacific Decadal Oscillation [PDO]), four wave parameters (significant wave height [H_s], mean wave period [T_m], and zonal [$D_{m,x}$] and meridional [$D_{m,y}$] wave direction components) and wind parameters (wind speed [WS_{10}], and zonal [u_{10}] and meridional [v_{10}] components). For this purpose, we regressed wind and wave parameters against the oscillation indices to create spatial composites of slope values, quantifying the correlation between wave parameters and indices. An EOF (empirical orthogonal function) analysis was also carried out to identify variability modes of wave parameters and to associate them to each climate index. The combining effects of ENSO and SAM were analysed by calculating H_s, T_m and wind speed anomalies for the periods in which the phases of these oscillations co-occur. We found important correlations not only with the dominant mode of variability, but also with secondary and even quaternary modes. For ENSO, negative correlations between the Oceanic Niño Index (ONI) and H_s, T_m, and $D_{m,x}$ in the northwest part of the South Atlantic Ocean were highlighted, with a decrease (increase) of up to 8 cm of H_s per ONI unit in El Niño (La Niña) events. We established positive correlations also between ONI and these wave parameters in subtropical regions along the western African coast during austral summer, which were intensified by negative SAM. During autumn, however, we observed La Niña positive H_s anomalies for this region, which were also intensified by negative SAM. Finally, we found new, significant correlations between South Atlantic Ocean wave climate and SAM. We determined that the PDO index has negative correlations with H_s and T_m, while directional components present stronger variability.

Keywords wave climate; South Atlantic Ocean; El Niño Southern Oscillation; Southern Annular Mode; Pacific Decadal Oscillation

1. Introduction

Energy transfers that take place at ocean–atmosphere interface are dynamical and involve a range of complex processes that link the smallest scales to the largest ones. Surface ocean waves are the outcome of exchange of energy and momentum between atmosphere and ocean. These wind-induced oscillations grow in size proportionally to wind speed, fetch and duration. Since many climate oscillations are reported to induce changes in sea level pressures and wind patterns, surface ocean waves are under the influence of both large-scale atmospheric circulation and climate teleconnections.

The influence of climate variability on wave climate has been well examined for the North Atlantic (Allan and Komar, 2006, 2000; Dodet et al., 2010; Gulev and Grigorieva, 2006; Woolf et al., 2002) and North Pacific oceans (Allan and Komar, 2006; Gulev and Grigorieva, 2006; Menéndez et al., 2008; Ruggiero et al., 2010). However, only a few studies have focused on the Southern Hemisphere, even though the region encompasses the Southern Ocean — Earth's most important area of swell generation (Young, 1999). One of the most significant studies of the influence of climate variability on wave climate in the Southern Hemisphere was conducted by Hemer et al. (2010), which found strong correlations between the Pacific Ocean wave climate and both the Southern Annular Mode (SAM) Index and the Southern Oscillation Index (SOI) — which are used for classifying the SAM and the El Niño–Southern Oscillation (ENSO), respectively, into their positive and negative phases. Marshall et al. (2018) extended the work of Hemer et al. (2010), reinforcing the important role of SAM on wave climate variability by analysing mean sea level pressure (MSLP), wind and wave anomalies. This most recent study also established links between SAM and ENSO. Both works, however, focused only on the Pacific Ocean region of the Southern Hemisphere.

Regional studies have also established links between wave climate and SOI: prior research suggesting a clockwise rotation of wave direction during negative anomalies of SOI are well documented for the Gold Coast at Queensland, Australia (Hemer et al., 2008; Phinn and Hastings, 1995; Ranasinghe et al., 2004). Significant correlations between variability modes of significant wave height and wind anomalies related to ENSO in the Southern New Zealand wave climate are also acknowledged (Laing, 2000). These works are comprehensive, but primarily focused on the Pacific Ocean, whilst the Southern Atlantic Ocean (SAO) remains comparatively understudied. To our knowledge, only four studies have directly examined the influence of climate variability in the wave climate of SAO at a range of spatial scales. Significant correlations between climate indices and direction of mean wave energy flux were found by Reguero et al. (2013), however, this study only analysed coastal regions of Latin America. Similarly, Pereira and Klumb-Oliveira (2015) correlated the Oceanic Niño Index (ONI) to significant wave height in the central area of the coastal zone of Rio de Janeiro, Brazil, associating larger waves to El Niño and smaller waves to La Niña. The other two works analysed wave climate variability offshore Santa Catarina, Brazil: Dalinghaus (2016) established links between ENSO, SAM, Pacific Decadal Oscillation (PDO), and wave parameters, while Oliveira (2017) found correlations between wave direction and SOI.

To explore variability and trends of surface waves across large regions of oceans without data gaps, climate reanalyses offer the most comprehensive dataset. Buoys also deliver consistent long-term data, but are usually discontinuously located and cover no more than the last three decades. Satellite altimetry provides global coverage since 1978, but only for significant wave height. Reanalyses, however, provide a spatially and temporally complete record of wave climate, some of them assimilating both observations and satellite altimetry measurements into their numerical models. Nevertheless, *in situ* observations are essential for calibration and validation of reanalysis datasets.

The understanding of wave climate and its relationship to large-scale climate modes is essential information for several fields, such as coastal management, marine biodiversity, renewable energy extraction, navigation and tourism. For instance, when surface ocean waves reach the coastline, they induce radiation stress gradients that result in longshore currents, the primary mechanism of sediment transport in the coastal zone. The magnitude of this process is influenced by large scale climate conditions. Surface ocean waves also have major impact in marine biodiversity by carrying nutrients to beaches and transforming habitats, for example. Surf related tourism has been growing in popularity in recent years, and trends regarding climate oscillations are a subject that tourist operators already keep in mind when planning. We focus here on the demand for a comprehensive study of wave variability associated to climate oscillations in the South Atlantic Ocean. By analysing wave data from the ERA5 reanalysis dataset, this study aims to provide statistical analyses of wave patterns during SAM, ENSO and PDO phases in order to show how these climate oscillations affect synoptic processes responsible for wave climate in SAO. This paper is organised as follows: Section 2 presents the relevant datasets; in Section 3 we introduce and discuss the relationship between wave patterns and climate oscillations; Section 4 describes the combined effects of ENSO and SAM. Conclusions are presented in Section 5. As the reader will find herein the use of many acronyms, a list of acronyms is supplied bellow for facilitating reading.

List of Acronyms

$D_{m,x}$: Zonal wave direction
$D_{m,y}$: Meridional wave direction
ENSO: El Niño–Southern Oscillation
EOF: Empiric Orthogonal Function
H_s: Significant wave height
kNN: k-Nearest Neighbours
MSLP: Mean Sea Level Pressure
ONI: Oceanic Niño Index
PC: Principal Component of the EOF
PDO: Pacific Decadal Oscillation
PDOI: Pacific Decadal Oscillation Index
SAM: Southern Annular Mode
SAMI: Southern Annular Mode Index
SAO: South Atlantic Ocean
SOI: Southern Oscillation Index
SST: Sea Surface Temperature
T_m: Mean wave period
T_p: Peak wave period
u_{10}: Zonal wind component
v_{10}: Meridional wind component
WS_{10}: Wind speed

2. Datasets

2.1. Climate indices

Climate indices are used to characterise climate oscillations in their respective phases, quantifying environmental factors such as MSLP and sea surface temperature (SST). The indices adopted here are ONI for ENSO, SAMI for SAM and PDOI for PDO. The source and calculation method to obtain each of these indices are described in Table 1.

Table 1 Climate indices details regarding the index author, calculation method and source

Index	*Reference*	*Calculation*	*Data Source:*
ONI	NOAA Climate Prediction Centre	The running 3-month average sea surface temperatures anomaly at the Niño 3.4 region (5°N-5°S, 120°-170°W)	http://origin.cpc.ncep.noaa.gov/products/analysis_monitoring/ensostuff/ONI_v5.php
SAMI	Marshall (2003)	Average of the zonal MSLP between 40°S and 65°S parallels	http://www.nerc-bas.ac.uk/icd/gjma/sam.html
PDOI	Mantua (1999)	The principal component of the first Northern Pacific Ocean SST variability mode	https://www.ncdc.noaa.gov/teleconnections/pdo/

2.2. Wave parameters and wind data

Significant wave height (H_s), mean wave period (T_m), peak wave period (T_p), mean wave direction (D_m), zonal (u_{10}) and meridional (v_{10}) components of 10 m wind direction were obtained from the ERA5 reanalysis dataset for the period between January 1979 and December 2019. The data was collected for the region comprising 15°N-60°S latitude and 75°W-30°E longitude. Wind speed (WS_{10}) was calculated from u_{10} and v_{10} wind components and zonal ($D_{m,x}$) and meridional ($D_{m,y}$) wave direction components were decomposed from D_m. The ERA5 reanalyses, developed by the European Centre for Medium-Range Weather Forecasts (ECMWF), is freely available and provides data from 1979 to the present, with hourly temporal resolution, 0.25° grid spacing for wind data, and 0.50° grid spacing for wave data. In ERA5, atmospheric data assimilation occurs in 12-hourly windows. Ocean waves are generated from atmosphere via surface wind stress. A two-way interaction is considered, where sea surface waves influence the atmospheric boundary layer. ERA5 also introduced a new wave advection scheme that compared to its predecessor, ERA-Interim, better resolves propagation along coastlines (Hersbach et al., 2020). The scatter index of significant wave height against buoy observations is much lower than the one of ERA-Interim for all locations assessed in the paper of Hersbach et al. (2020).

2.3. Buoy data

In order to assess the quality of ERA5 reanalysis wave data for our region of interest, statistical measures were applied to verify the correlation between reanalysis parameters and observations. Here, observations were obtained from buoys along the Brazilian coast. Seven different buoy sites located on open coastline were chosen for the validation: Cabo Frio, Fortaleza, Itajaí, Recife, Rio Grande, Santos and Vitória. Figure 1 displays buoy locations plotted against the General Bathymetric Chart of the Oceans 2020 grid (GEBCO Compilation Group, 2020), and Table 2 presents buoy additional information.

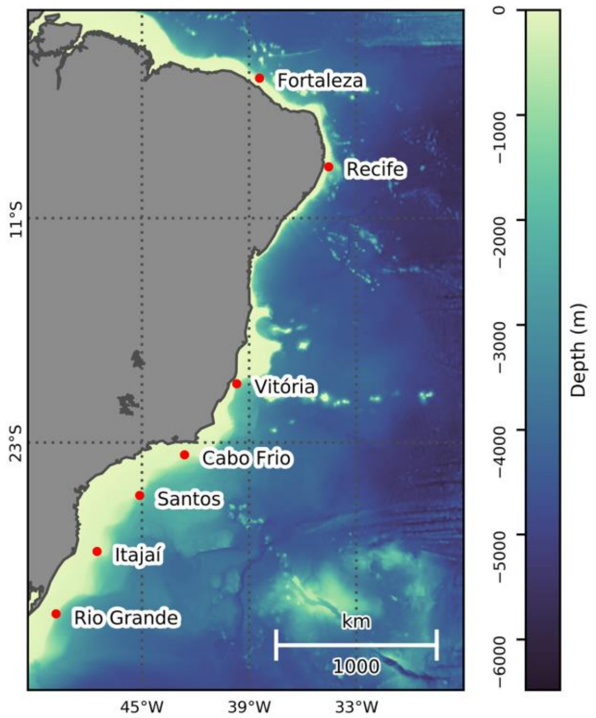

Figure 1 Buoy locations and GEBCO bathymetry

To reduce observational uncertainty and noise, buoy measurements were filtered for outliers due to measurement errors by using the k-Nearest Neighbours (kNN) algorithm from the PyOD Python toolkit (Zhao et al., 2019). For kNN, given an observation, the distance to its k-th nearest neighbour is interpreted as an outlier score (Angiulli and Pizzuti, 2002; Ramaswamy et al., 2000). The relation between H_s and T_p was assessed by the algorithm in order to classify the outliers with contamination rate set to 0.01. A scatter plot showing the kNN decision function, inliers and outliers, as well as the buoy timeseries before and after the retrieval of outliers, is demonstrated in Figure 2. It is important to mention that even though this approach is important, it is subject to classifying correct observations as outliers. However, as Figure 2 indicates, kNN delivered a good performance. After removing outliers, for each of the selected sites, the corresponding nearest grid point was extracted from ERA5 dataset and compared to the buoy timeseries through Pearson's correlation test, providing a measure of linear correlation for the reanalysis wave dataset. The analysed period is described in Table 2.

Table 2 Buoy location and period of available data

Site name	*Latitude*	*Longitude*	*Depth*	*Start date*	*Final available date*	*Number of hourly samples*
Cabo Frio	-23.63°	-42.63°	142 m	2016-07	2017-10	3,905
Fortaleza	-3.21°	-38.43°	357 m	2016-11	2017-12	2,408
Itajaí	-28.48°	-47.52°	182 m	2009-04	2017-07	22,270
Recife	-8.15°	-34.56°	165 m	2012-09	2016-04	12,469
Rio Grande	-31.52°	-49.81°	241 m	2011-02	2017-06	21,489
Santos	-25.70°	-45.14°	522 m	2011-04	2017-07	47,918
Vitória	-19.93°	-39.70°	281 m	2015-10	2017-07	14,065

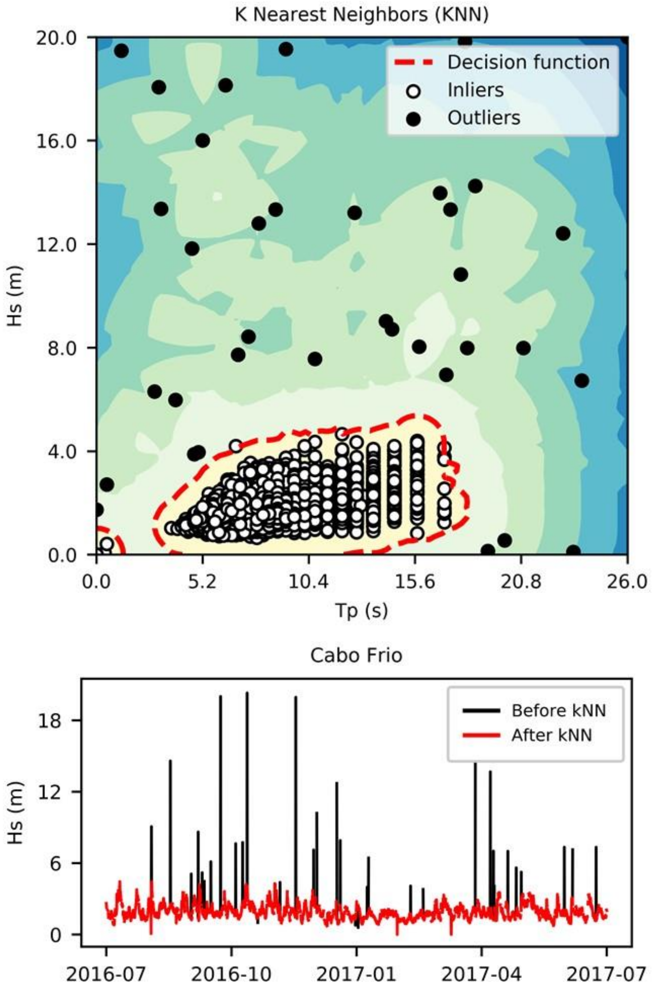

Figure 2 Decision function based on kNN algorithm separating inliers from outliers for the buoy of Cabo Frio (top). Cabo Frio H_s timeseries before and after kNN processing (bottom).

The ERA5 timeseries correlates well to wave observations, with a slight underestimation of maximum values and overestimation of minimum values, especially at Fortaleza and Recife. Wave parameters have the highest correlation at Cabo Frio, with a correlation coefficient R=0.92 for H_s (Fig. 3a), R=0.77 for T_p (Fig. 3b) and R=0.91 for D_m (Fig. 3c). The lowest correlation is found at Recife, where coefficients are significant, but the R value found for T_p is 0.52 (Figs. 3d–f). The T_p correlations were weaker when compared to other parameters. Even though outliers were eliminated, this is likely because buoy T_p is an instantaneous measure recorded in discrete time intervals. In addition to this, especially T_p, but also H_s and D_m presented smaller R values at the buoys located in north-east Brazilian coast (Fortaleza and Recife), where the continental shelf is narrower and steeper when compared to the other locations (Fig. 1), leading to an abrupt evolution of waves due to shallow water transformation processes. Still regarding wave transformation processes, another limitation of this analysis is the potential for wave direction to change due to refraction in the shallow waters in which Waverider buoys are positioned. This might have introduced a small bias between the buoy wave direction data and ERA5 reanalyses in some locations. To improve future results, buoy wave directions could be inversely ray-traced into deep water, following the methods described by Hemer et al. (2010). Despite these limitations, all p-values remain smaller than 0.001, indicating valid correlations. Results of this analysis are presented in Table 3.

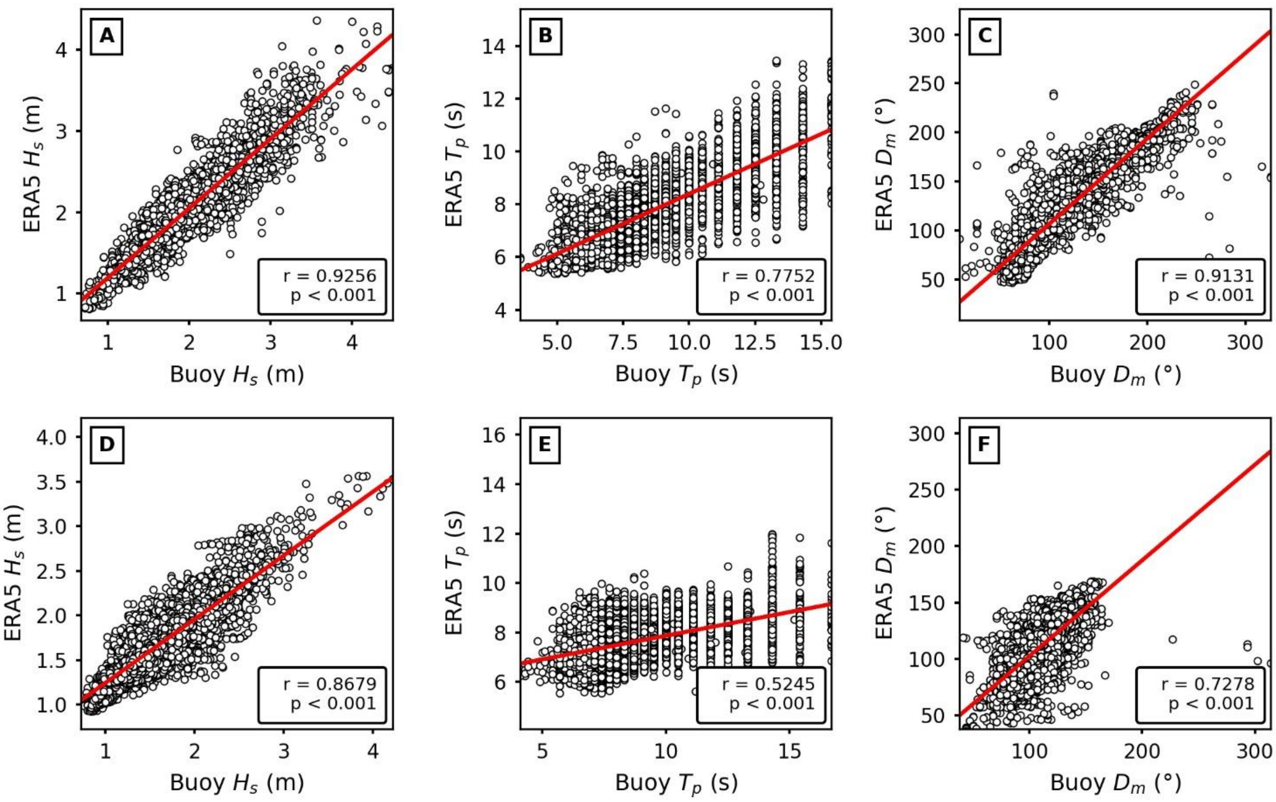

Figure 3 Graphic analysis of correlation between wave parameters of ERA5 reanalyses and buoy observations for significant wave height (A and D), peak wave period (B and E) and mean wave direction measured in degrees clockwise from True North (C and E) at Cabo Frio (A–C) and Recife (D–F). Trendline is plotted in red.

Table 3 Validation results where H_s is significant wave height measured in metres, T_p is mean wave period measured in seconds, and D_m is mean wave direction measured in degrees clockwise from True North. “min” represents minimum and “max” represents maximum values registered

Site	*Wave parameter*	*Waverider buoy*			*ERA5*			*p*	*R*
		min	*mean*	*max*	*min*	*mean*	*max*		
Cabo Frio	H_s	0.7 m	1.9 m	4.5 m	0.8 m	2.0 m	4.4 m	<0.001	0.92
	T_p	3.6 s	9.3 s	15.4 s	5.3 s	8.0 s	13.4 s	<0.001	0.78
	D_m	8.0°	123.1 °	326.0°	46.9°	126.7°	249.2°	<0.001	0.91
Fortaleza	H_s	0.8 m	1.5 m	2.7 m	1.0 m	1.7 m	2.5 m	<0.001	0.86
	T_p	3.6 s	9.6 s	20.0 s	5.5 s	7.7 s	13.6 s	<0.001	0.68
	D_m	2.0°	57.5°	323.0°	1.23°	59.8°	134.6°	<0.001	0.82
Itajaí	H_s	0.6 m	2.0 m	5.5 m	0.7 m	2.0 m	5.6 m	<0.001	0.92
	T_p	3.7 s	9.4 s	18.2 s	5.0 s	7.8 s	13.6 s	<0.001	0.72
	D_m	1.0°	122.2°	329.0°	0.1°	123.8°	317.5°	<0.001	0.92
Recife	H_s	0.7 m	1.6 m	4.2 m	0.9 m	1.6 m	3.6 m	<0.001	0.87
	T_p	4.1 s	8.8 s	16.7 s	5.2 s	7.6 s	12.0 s	<0.001	0.52
	D_m	38.0°	108.7°	314.0°	27.7°	109.9°	169.0°	<0.001	0.72
Rio Grande	H_s	0.6 m	2.1 m	5.9 m	0.7 m	2.0 m	6.0 m	<0.001	0.92
	T_p	3.6 s	9.0 s	16.8 s	4.9 s	7.7 s	12.8 s	<0.001	0.72
	D_m	2.0°	119.5°	329.0°	2.3°	118.2°	327.1°	<0.001	0.93
Santos	H_s	0.7 m	1.9 m	5.4 m	0.8 m	1.9 m	5.5 m	<0.001	0.92
	T_p	3.9 s	9.5 s	20.0 s	4.9 s	8.1 s	13.8 s	<0.001	0.72
	D_m	1.0°	131.9°	330.0°	1.5°	129.8°	328.9°	<0.001	0.91
Vitória	H_s	0.6 m	1.5 m	4.0 m	0.8 m	1.6 m	3.7 m	<0.001	0.90
	T_p	3.4 s	9.0 s	20.0 s	5.0 s	7.6 s	13.6 s	<0.001	0.70
	D_m	9.0°	103.0°	244.0°	15.1°	113.4°	198.8°	<0.001	0.90

3 Wave climate patterns regarding climate oscillations

For correlating wave and wind parameters to climate indices, data was first separated into meteorological seasons by grouping the monthly means of December, January and February for summer; March, April and May for autumn; June, July and August for winter; and September, October and November for spring. Wave and wind parameters were linearly regressed against climate indices, and wave and wind seasonal climatologies were calculated by seasonally averaging these parameters. Composites were created by plotting the slope of the linear regression, the *p*-value, and the climatology of the analysed parameter to the Equidistant Cylindrical Projection of Matplotlib Basemap toolkit (Hunter, 2007).

To further analyse the influence of climate oscillations on wave climate variability, EOF (empirical orthogonal function) analyses were performed on seasonal wave parameter data to identify wave variability modes and correlate their principal components (PCs) to climate indices (Dawson, 2016). Before computing the EOFs, anomalies of wave parameter data were calculated by subtracting the 40-year mean seasonal value from the actual seasonal mean. Their long-term tendencies were also removed by subtracting the linear least-squares fit from the data. Thus, all that was left was the variability related neither to long-term cycles (such as climate warming) nor to seasonal signals, making it possible to interpret the remaining variability modes as products of the influence of climate oscillations. It is important to note, however, that the following results are not categorical and absolute: Section 4 will explore the combined effects of ENSO and SAM, showing how the wave state varies depending on the combination of ENSO and SAM phases.

3.1 El Niño–Southern Oscillation patterns

As we have seen in Section 2.1, ONI is an indicator of the ENSO phase, which, within the context of this index, can be in one of three different phases: negative, positive or neutral. ENSO is a coupled atmosphere–ocean phenomenon where SST anomalies are observed over the Equatorial region of Pacific Ocean (Niño 3.4 Region) during the two active ENSO phases (La Niña and El Niño). MSLP surface anomalies also occur together with these SST anomalies, in an atmosphere-ocean positive feedback process denominated Bjerknes feedback (Bjerknes, 1966). Resultant changes in the convection pattern over Equator caused by this positive feedback modulate Rossby waves, extending the changes in MSLP and wind regime into temperate latitudes (Bhaskaran and Mullan, 2003).

Due to the orientation of Brazilian coast, the southern swell has limited impact over low latitudes of western SAO. Except for austral spring and summer, when the North Atlantic Ocean swell arrives to the region, the north-west of SAO is dominated by seas characterised by east direction (Reguero et al., 2013; Young, 1999). Along equatorial line, the northern Brazilian coast displays positive correlations between H_s, $D_{m,y}$ and ONI and negative correlations between T_m, $D_{m,x}$ and ONI during austral autumn (Fig. 4). This translates into waves with shorter T_m (up to -0.18 s per ONI, R=-0.39) (Fig. 5b) yet larger H_s (up to 8 cm per ONI, R=0.54) (Fig. 5a) and stronger north-eastern component as ONI becomes increasingly positive, and the opposite as ONI gets negative, suggesting the favouring of trade wind seas during El Niño (positive ONI) and hindering of trade wind seas during La Niña (negative ONI). This finding is also supported by significant correlations between u_{10}, v_{10}, WS_{10} and ONI along equatorial line (Fig. 6): trade winds are enhanced (positive ONI) or dampened (negative ONI) by up to 60 cm/s per ONI. The more positive ONI is, the more the enhanced trade winds strengthen trade-wind swell in the north-west SAO, leading to larger H_s. These results are interesting, since the literature usually associates El Niño events to the weakening of Walker Circulation, resulting in dampening of trade winds over the Pacific Ocean (Aragão, 1998, 1986; Kousky et al., 1984; Souza and Ambrizzi, 2002). However, our study shows that trade winds are intensified for the west Equatorial Atlantic region and dampened for the east Equatorial Atlantic region during austral autumn and winter, even though ENSO usually peaks in austral summer (Chen and Jin, 2020).

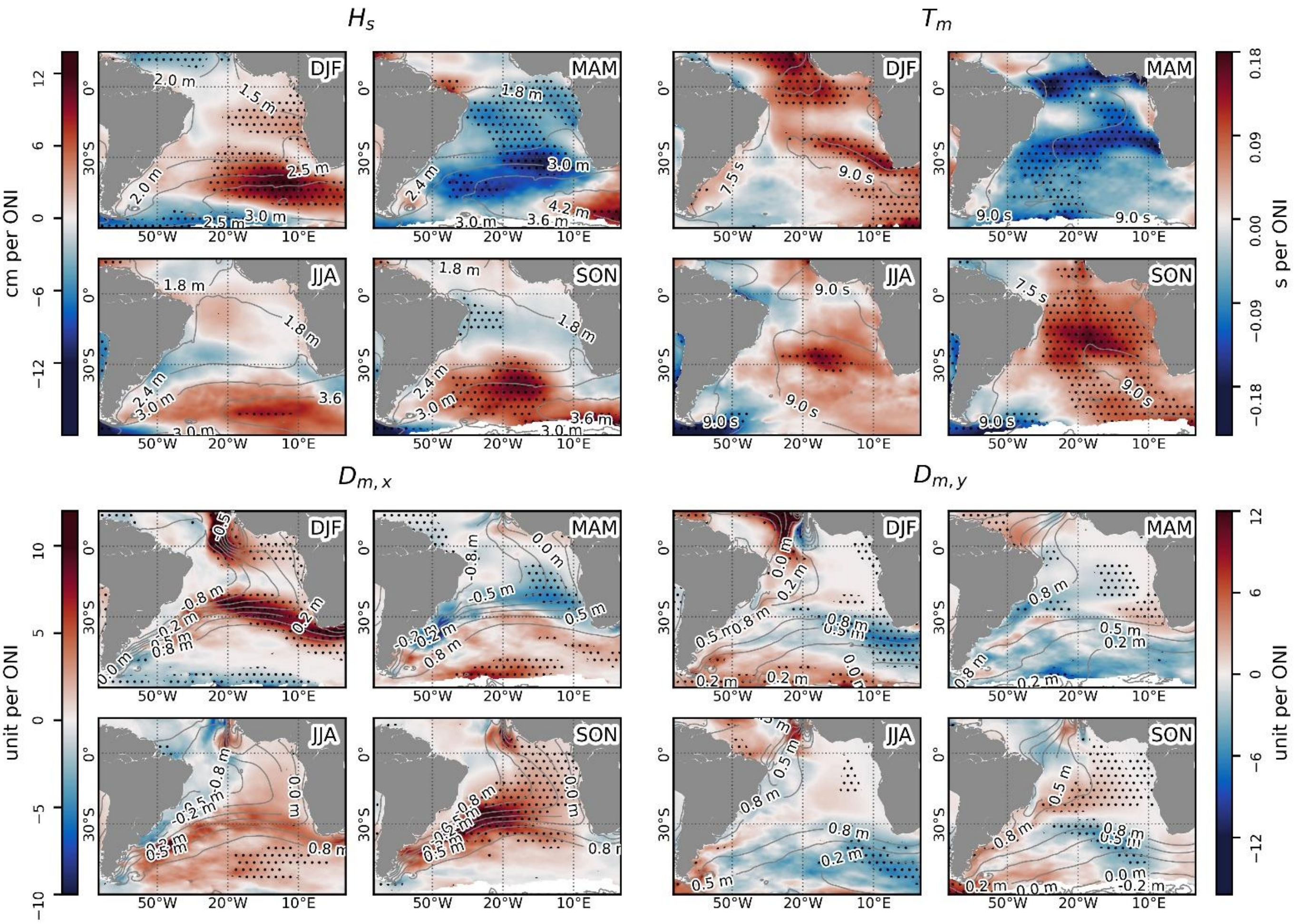

Figure 4 Seasonal composites of significant wave height (H_s), mean wave period (T_m), zonal component of wave direction ($D_{m,x}$) and meridional component of wave direction ($D_{m,y}$) regressed against Oceanic Niño Index. Climatologies are plotted in grey contour levels, and significant positive and negative correlations at 90% confidence level (p<0.10) are hatched with black dots. DJF stands for December, January, February (austral summer), MAM for March, April, May (austral autumn), JJA for June, July, August (austral winter) and SON for September, October, November (austral spring).

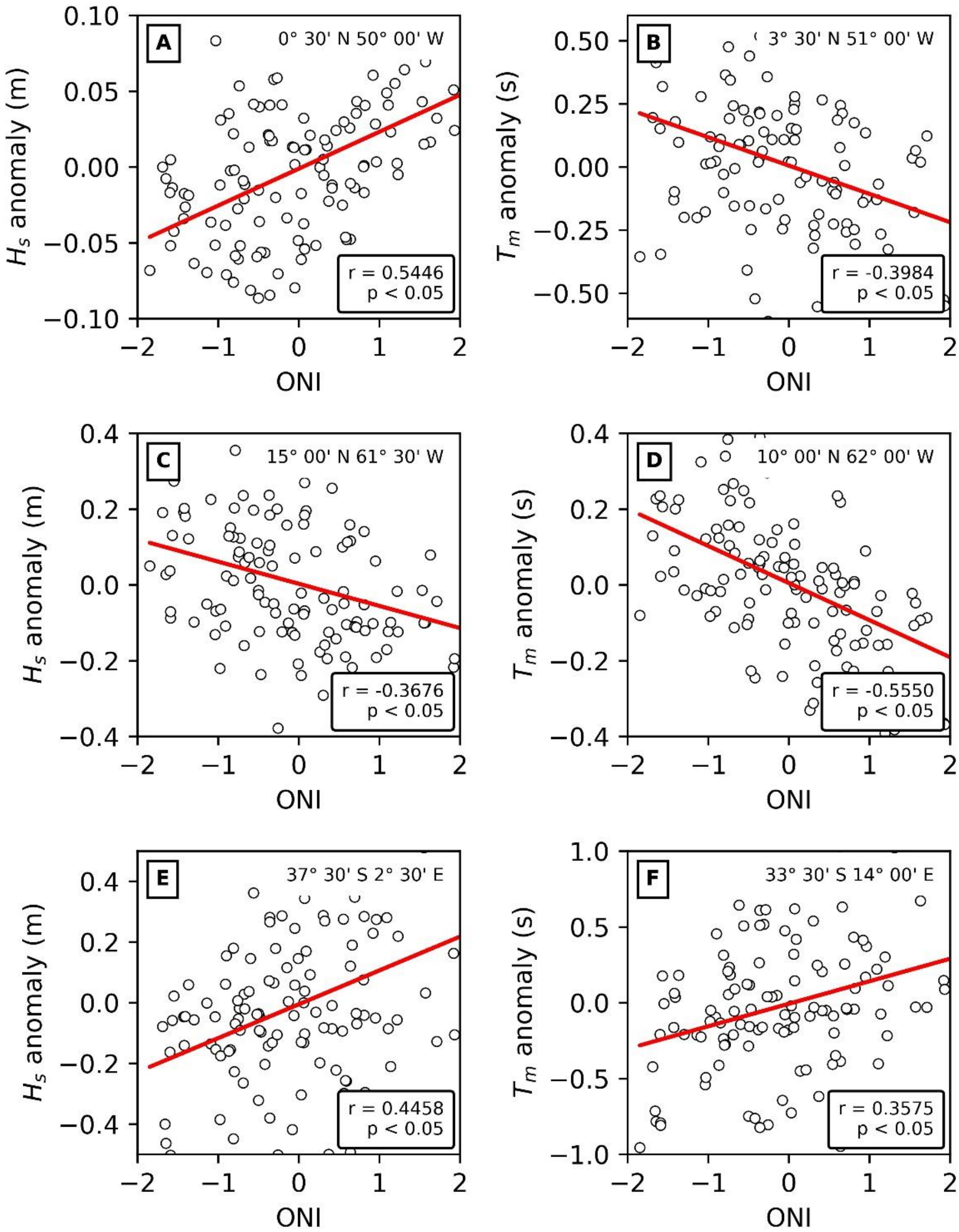

Figure 5 Graphic analysis of correlation between summer anomalies of wave parameters and ONI at selected locations. Trendline is plotted in red.

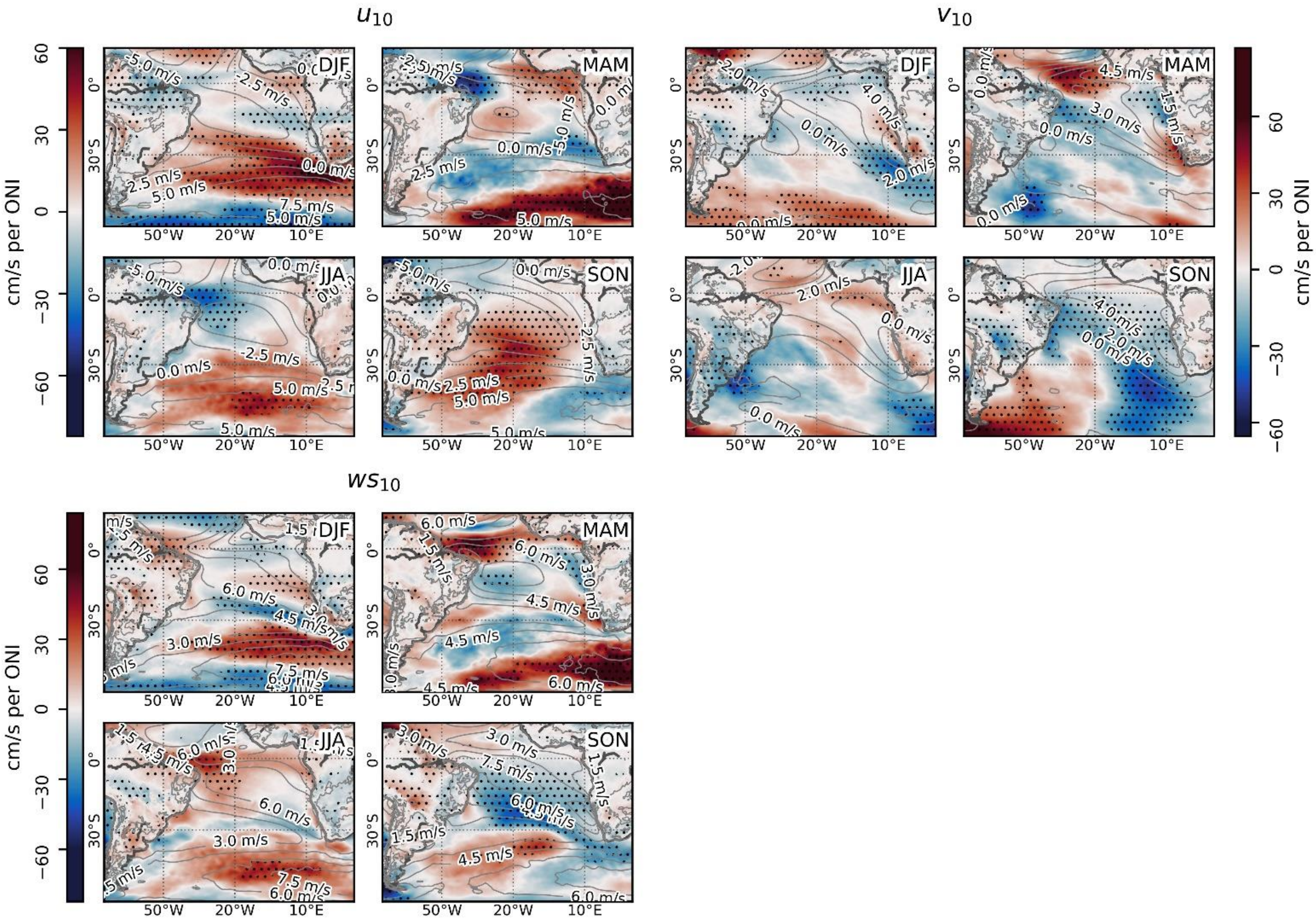

Figure 6 Seasonal composites of zonal and meridional components of 10 m wind (u_{10} and v_{10}, respectively) and wind speed (WS_{10}) regressed against Oceanic Niño Index. Climatologies are plotted in grey contour levels, and significant positive and negative correlations at 90% confidence level (p<0.10) are hatched with black dots. DJF stands for December, January, February (austral summer), MAM for March, April, May (austral autumn), JJA for June, July, August (austral winter) and SON for September, October, November (austral spring).

During austral spring and summer, the swell originated from polar lows in the North Atlantic (Semedo et al., 2009; Young, 1999) reaches the low latitudes of the Atlantic Ocean. For summer, Figure 4 shows increase of H_s (Fig. 5c), T_m (Fig. 5d) and $D_{m,x}$ and decrease of $D_{m,y}$ with negative ONI in the low latitudes of western Atlantic Ocean. The opposite is observed for positive ONI. These correlations suggest stronger North Atlantic swell signals as ONI becomes negative and weaker North Atlantic swell signals as ONI transitions into its positive phase. This assumption is supported by the fact that La Niña events are associated with anomalously negative MSLP in the north of 50°N in January and February, with a stronger polar vortex (Moron and Gouirand, 2003). The opposite of this is observed for El Niño. Recent studies have found negative correlations between ONI and the North Atlantic Oscillation, which also presents a pattern of negative MSLP anomalies (Hardiman et al., 2019; Iza et al., 2016; Zhang et al., 2019). As the North Atlantic oscillation has already been observed to modulate H_s (Gulev and Grigorieva, 2006; Semedo et al., 2009), the correlations found here for H_s, T_m, $D_{m,x}$ and $D_{m,y}$ are a possible reflection of the trans-basin tele-connections between ONI, the North Atlantic Oscillation, and the North Atlantic swell.

Except for austral autumn, the south-eastern sector of SAO (below 30°S) shows positive correlations between H_s, T_m, $D_{m,x}$ and ONI (Fig. 4). A possible driver of this is the enhancement of the subtropical jet stream (Bhaskaran and Mullan, 2003; Held et al., 1989; Karoly, 1989; Zimmermann, 2017) during El Niño events, favouring the development of mid-latitude cyclones and stronger westerlies. During La Niña years, however, the subtropical jet stream is weakened, as well as the frequency of mid-latitude cyclones. The increase in H_s (Fig. 5e), T_m (Fig. 5f), and $D_{m,x}$ in south-eastern SAO with higher ONI (Fig. 4) is coherent to the increased frequency of extra-tropical cyclones and stronger westerlies, driving larger and more westerly waves when ONI is higher (El Niño) and smaller and more easterly waves when ONI is lower (La Niña) (Fig. 4). Along the western African coast, however, negative correlations between these parameters and ONI are observed during austral autumn, leading to larger H_s and T_m with lower ONI (Fig. 4).

Selected principal components of variability modes returned from the EOF analysis correlate well to ONI (bold values in Table 4). The second variability mode of summer H_s, the third variability mode of autumn H_s and the fourth variability modes of both winter and spring H_s are associated to ONI (Fig. 7). Regarding $D_{m,x}$ and $D_{m,y}$, significant correlations were found with the PCs of EOF 4 of summer $D_{m,x}$, EOF 2 of spring $D_{m,x}$, EOF 2 of summer $D_{m,y}$ and EOF 3 of spring $D_{m,y}$ (Fig. 7). The parameter T_m had its third mode of summer and autumn, second of winter and fourth of spring significantly correlating to ONI. The spatial patterns of these variability modes are notably similar to the ones found for correlation composites between wave parameters and ONI.

Table 4 Module of correlation coefficients (|R|) between climate indices (ONI, PDO and SAMI) and principal components associated to variability modes (EOF) of each wave parameter (WP). VF is the total variance fraction accounted for by each EOF mode. Values in bold represent significance values at 95 % level ($p < 0.05$)

WP	Season	EOF	VF %	$\vert R\vert$ ONI	$\vert R\vert$ PDO	$\vert R\vert$ SAMI	EOF	VF %	$\vert R\vert$ ONI	$\vert R\vert$ PDO	$\vert R\vert$ SAMI
H_s	Summer	1	27	0.03	0.06	0.21	3	11	0.09	0.04	0.00
		2	22	**0.35**	**0.21**	**0.45**	4	06	0.02	0.10	0.08
	Autumn	1	40	0.08	0.07	0.10	3	10	**0.22**	0.06	**0.30**
		2	14	0.12	0.09	**0.39**	4	07	0.15	0.19	**0.23**
	Winter	1	30	0.12	**0.26**	**0.26**	3	13	**0.19**	0.12	0.14
		2	15	0.15	0.21	**0.29**	4	10	**0.24**	0.00	0.07
	Spring	1	46	0.11	0.06	**0.24**	3	09	0.09	0.10	0.12
		2	12	0.13	0.06	**0.52**	4	08	**0.24**	**0.22**	0.02
T_m	Summer	1	36	0.12	0.01	0.06	3	12	**0.20**	**0.20**	**0.34**
		2	16	0.01	0.03	0.05	4	08	0.12	0.17	0.07
	Autumn	1	36	0.03	**0.22**	0.08	3	10	**0.22**	0.16	**0.35**
		2	23	0.11	0.02	0.05	4	06	0.08	0.03	**0.20**
	Winter	1	43	**0.19**	**0.30**	0.09	3	08	0.00	**0.25**	**0.20**
		2	15	**0.21**	0.03	**0.36**	4	07	**0.19**	**0.18**	0.05
	Spring	1	39	**0.19**	0.08	0.17	3	11	**0.26**	**0.30**	**0.21**
		2	17	0.05	0.13	0.10	4	06	**0.28**	**0.32**	0.12
$D_{m,x}$	Summer	1	26	**0.22**	0.13	**0.23**	3	07	0.08	0.05	0.07

WP	Season	EOF	VF %	|R| ONI	|R| PDO	|R| SAMI	EOF	VF %	|R| ONI	|R| PDO	|R| SAMI
		2	17	0.05	0.13	**0.24**	4	06	**0.33**	0.14	**0.28**
	Autumn	1	25	0.04	0.03	**0.18**	3	10	0.05	0.10	0.12
		2	17	0.09	0.00	0.13	4	08	0.04	0.13	0.04
	Winter	1	25	0.14	0.06	0.06	3	11	**0.18**	0.02	0.11
		2	22	0.13	0.06	0.01	4	07	0.00	0.00	**0.22**
	Spring	1	25	**0.21**	**0.23**	0.10	3	08	0.02	0.06	0.02
		2	20	**0.24**	0.00	0.17	4	06	0.09	0.00	**0.33**
	Summer	1	19	**0.18**	0.00	0.02	3	09	0.16	0.13	0.17
		2	12	**0.24**	**0.26**	**0.60**	4	05	0.05	0.00	0.13
	Autumn	1	19	0.00	0.02	**0.31**	3	12	0.07	0.13	0.14
$D_{m,y}$		2	13	0.05	0.06	0.13	4	08	0.08	0.00	**0.47**
	Winter	1	22	0.06	0.04	0.11	3	10	0.05	0.06	0.13
		2	15	0.07	0.07	0.00	4	09	0.13	0.14	0.04
	Spring	1	26	0.03	0.14	0.16	3	12	**0.25**	**0.22**	**0.25**
		2	12	0.00	0.04	0.09	4	06	0.13	0.21	**0.23**

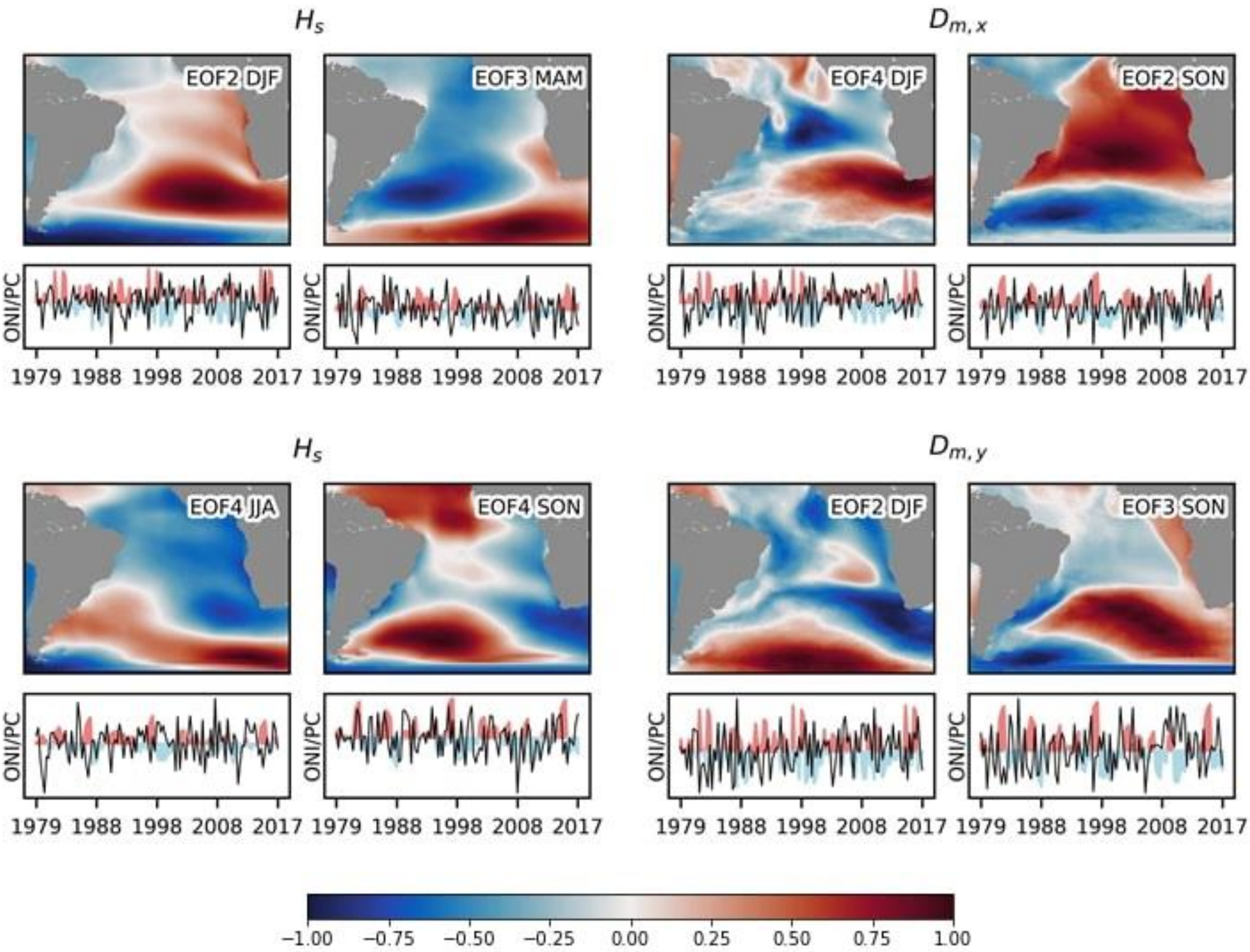

Figure 7 Seasonal composites of selected variability modes of significant wave height (left) and zonal and meridional wave components of wave direction (right). The principal component of the corresponding variability mode is plotted under its respective correlation map, in front of Oceanic Niño Index, which is plotted as anomaly plot. DJF stands for December, January, February (austral summer), MAM for March, April, May (austral autumn), JJA for June, July, August (austral winter) and SON for September, October, November (austral spring).

3.2 Pacific Decadal Oscillation patterns

Figure 8 demonstrates a prevalence of negative correlations between PDO index and H_s, and between the index and T_m, leading to an increase of H_s up to 10 cm per PDOI during negative phases of the oscillation and a decrease of H_s of the same magnitude during positive ones (Fig. 9a-b). These findings are congruent to the outcomes of Pezza et al. (2007) work. In their paper, it was shown that negative PDO events are associated to higher frequency of cyclonic activity over Antarctica and weaker than average anticyclones in subtropical latitudes, promoting the development of low-pressure systems over these regions. The increase in both H_s and T_m in negative PDO events are coherent with lower pressures and higher wind speeds in SAO triggered by this PDO phase. During summer, however, wave patterns are similar to ENSO correlation patterns: in temperate latitudes waves acquire westerly components (Fig. 8) with a larger index, as well as a larger H_s and T_m (Fig. 9c-d).

EOFs whose PCs have their best correlation coefficients with PDO are mostly the ones that also have their best correlation coefficients with ENSO (Table 4). This is not surprising because even though PDO and ENSO operate in different time scales, a negative event of PDO produces atmospheric circulation patterns similar to a negative event of ENSO; likewise, a positive PDO presents circulation patterns similar to a positive ENSO (Gershunov and Barnett, 1998; Mantua and Hare, 2002; Zhang et al., 1997). Thus, the effects of both oscillations on wave climate tend to be alike.

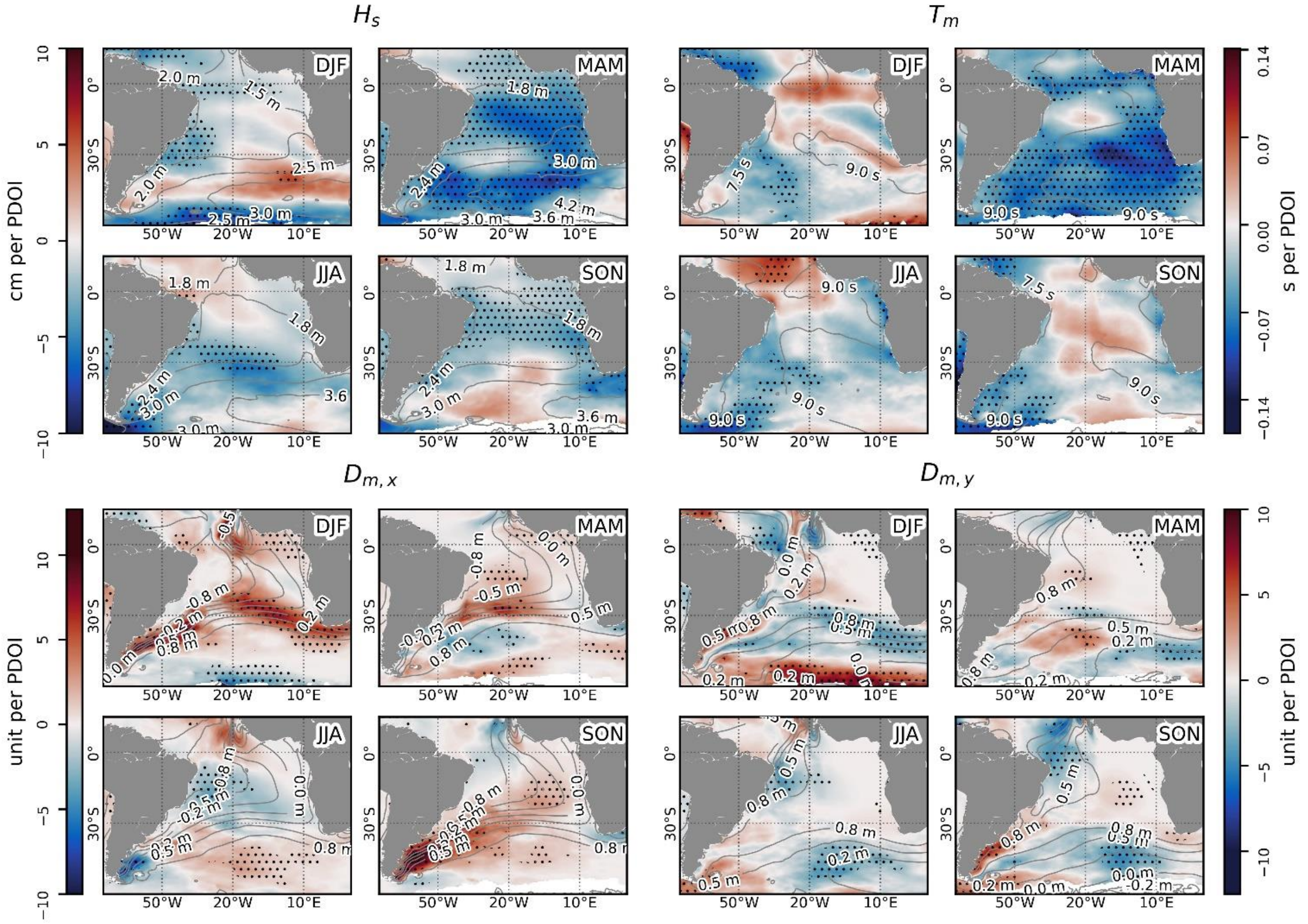

Figure 8 Seasonal composites of significant wave height (H_s), mean wave period (T_m), zonal component of wave direction ($D_{m,x}$) and meridional component of wave direction ($D_{m,y}$) regressed against Pacific Decadal Oscillation Index. Climatologies are plotted in grey contour levels, and significant positive and negative correlations at 90% confidence level ($p<0.10$) are hatched with black dots. DJF stands for December, January, February (austral summer), MAM for March, April, May (austral autumn), JJA for June, July, August (austral winter) and SON for September, October, November (austral spring).

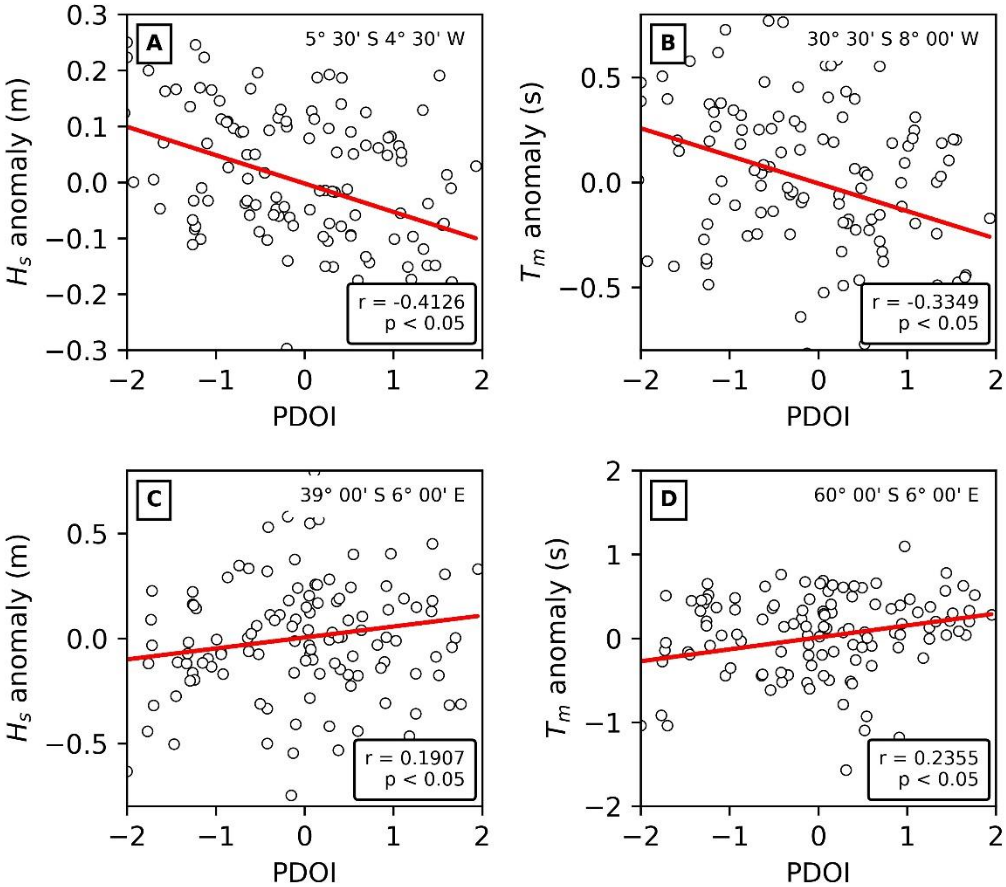

Figure 9 Graphic analysis of correlation between autumn (**A** and **B**) and summer (**C** and **D**) anomalies of wave parameters and PDOI at selected locations. Trendline is plotted in red.

3.3 Southern Annular Mode patterns

Figure 10 demonstrates significant correlations between wave fields and SAMI, opposing the findings of Hemer et al. (2010) that indicated a lack of SAM-related variability in SAO. One significant difference between our work and the work of Hemer et al. (2010) is the use of a third-generation reanalysis dataset from our side, with higher temporal and spatial resolutions. An increase in H_s with higher SAMI is observed in the southernmost latitudes (below 45° S) during spring and summer and along the Brazilian coast in summer (Fig. 11a-b). Between 30° S and 45° S, however, the eastern SAO and the Argentinian coast shows an increase in both H_s and T_m (Fig 11c-d) with lower SAMI during spring and summer (Fig. 10). In winter, when the storm belt is naturally displaced northward, SAM presented little effect on the wave climate. These correlations reflect the movement of the Southern Ocean storm belt during positive and negative phases of SAM. During a positive SAM, the storm belt contracts toward Antarctica. The contraction enhances the polar jet stream and drives strong westerly winds in higher latitudes (Limpasuvan and Hartmann, 2000; Thompson and Wallace, 2000). In temperate latitudes, conversely, positive SAM leads to increasing

MSLP, which undermines the development of mid-latitude cyclones (Carvalho et al., 2005; Limpasuvan and Hartmann, 2000; Thompson and Wallace, 2000) at the region, a synoptic type associated to larger waves. Consequently, smaller waves are observed in subtropical and temperate latitudes during a positive SAM. Negative SAM, however, causes expansion of the ocean storm belt toward the Equator, weakening winds in southernmost latitudes but promoting the development of synoptic types associated to low MSLP in temperate latitudes (Limpasuvan and Hartmann, 2000; Thompson and Wallace, 2000), which leads to larger waves propagating further north.

These patterns are also observed in the EOF analysis. The second variability mode of summer and spring H_s displays this bimodal pattern between high- and mid-latitudes (Fig. 12). Furthermore, a pattern similar to the positive correlation pattern along the Brazilian coast is also observed in the EOF 2 of summer. The EOF 2 of autumn and the EOF 2 of winter display a zonal bimodal pattern which is also observed in the correlation composites (Fig. 10). The correlation coefficients between the PCs of EOFs 2 of H_s in all seasons and SAMI are significant and considerably high (Table 4).

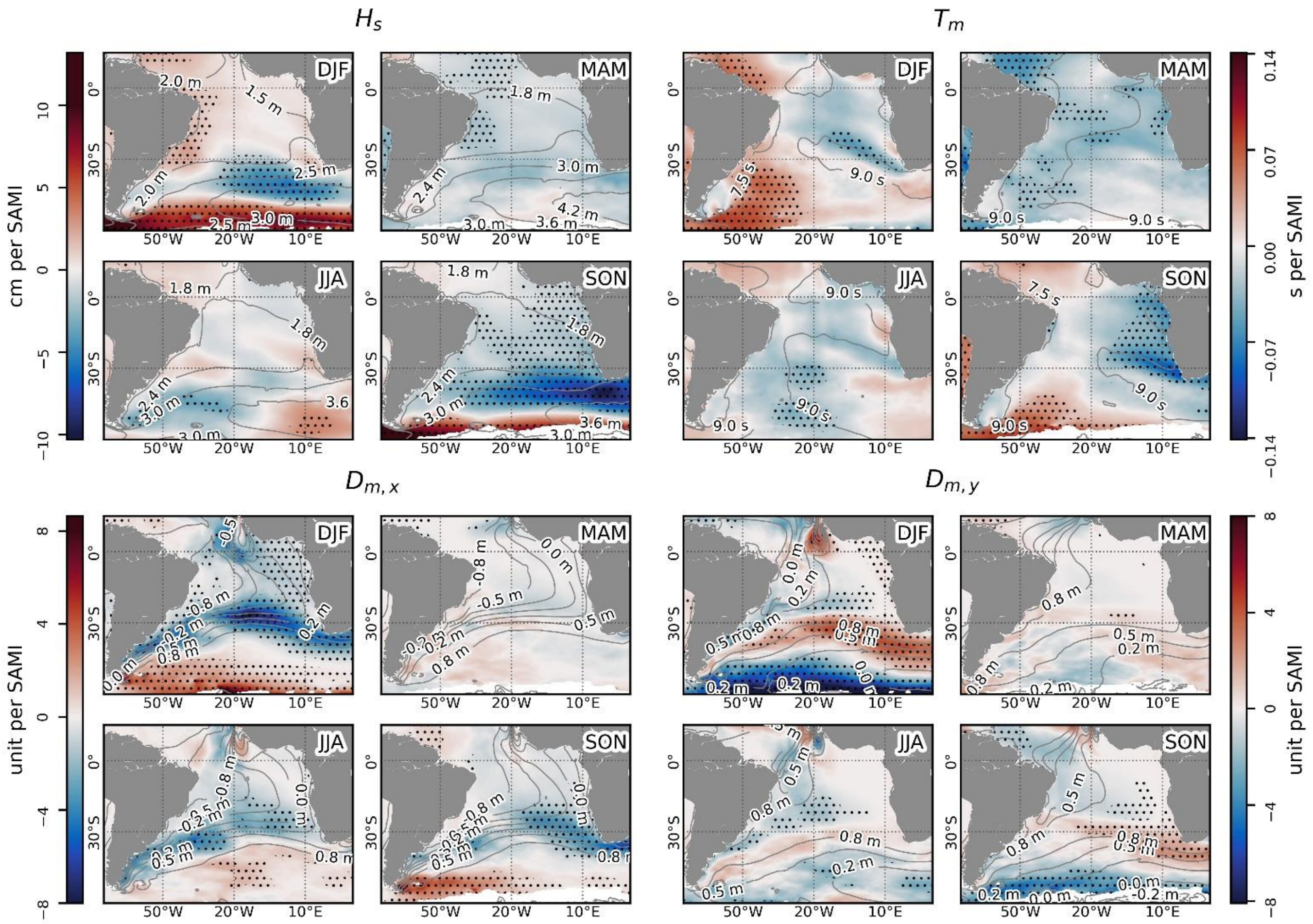

Figure 10 Seasonal composites of significant wave height (H_s), mean wave period (T_m), zonal component of wave direction ($D_{m,x}$) and meridional component of wave direction ($D_{m,y}$) regressed against Southern Annular Mode Index.

Climatologies are plotted in grey contour levels, and significant positive and negative correlations at 90% confidence level (p<0.10) are hatched with black dots. DJF stands for December, January, February (austral summer), MAM for March, April, May (austral autumn), JJA for June, July, August (austral winter) and SON for September, October, November (austral spring).

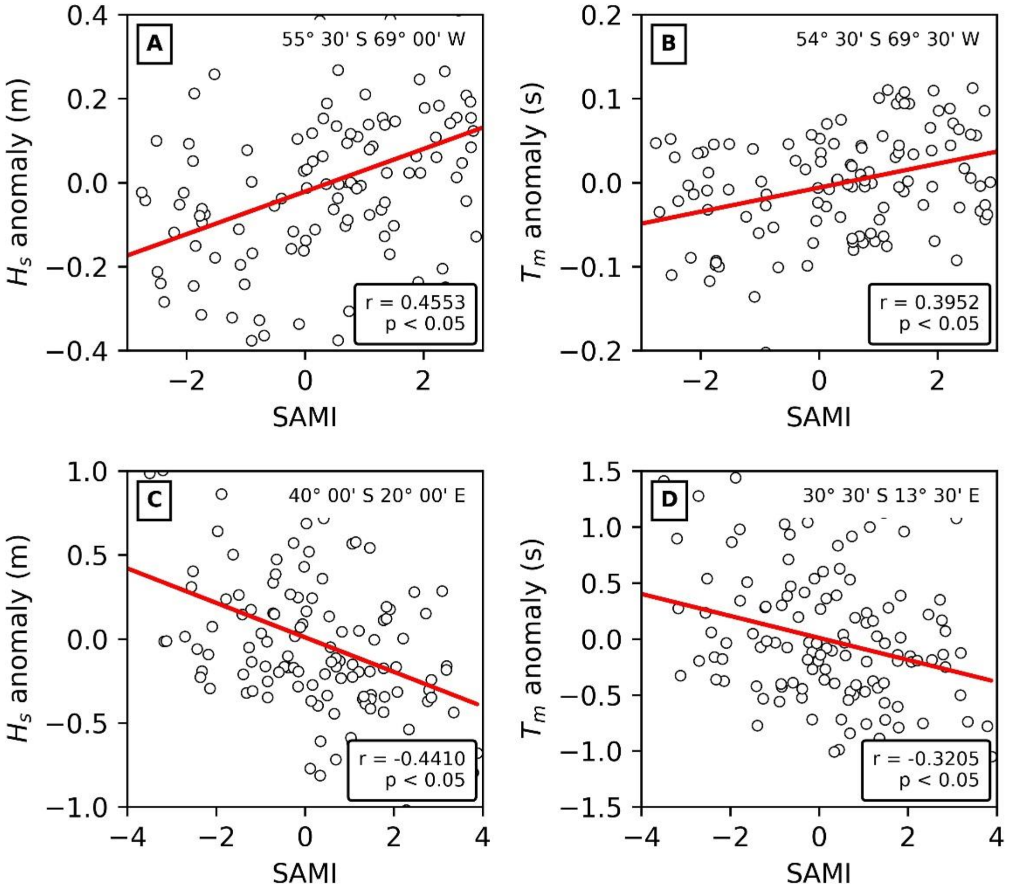

Figure 11 Graphic analysis of correlation between summer (**A** and **B**) and spring (**C** and **D**) anomalies of wave parameters and SAMI at selected locations. Trendline is plotted in red.

The changing position of low-pressure systems is also capable of acting over wave direction (Hemer et al., 2010). Indeed, positive correlations with $D_{m,x}$ (Fig. 10) were obtained for latitudes higher than 50°S during spring and summer, and in north-west SAO for all seasons, whereas negative correlations were observed in latitudes lower than 50°S in spring and summer, especially along the western African coast, forming a dipole with the southern part of South America. The parameter $D_{m,y}$ maintains its pattern of negative correlations in high latitudes and positive correlations in mid-latitudes during all seasons. Hence, with a more positive SAM, waves acquire a north-westerly component in latitudes higher than 50°S and in north-western SAO, and a south-easterly component with larger ONI in latitudes lower than 50°S and along the western African coast. SAMI and u_{10} correlation composites demonstrate the very same patterns (Fig. 13), indicating wave direction as consequence of wind direction during SAM phases. EOFs of $D_{m,x}$ and $D_{m,y}$

that presented the highest correlation coefficients with climate indices (Table 4) also reflect these patterns (Fig. 12).

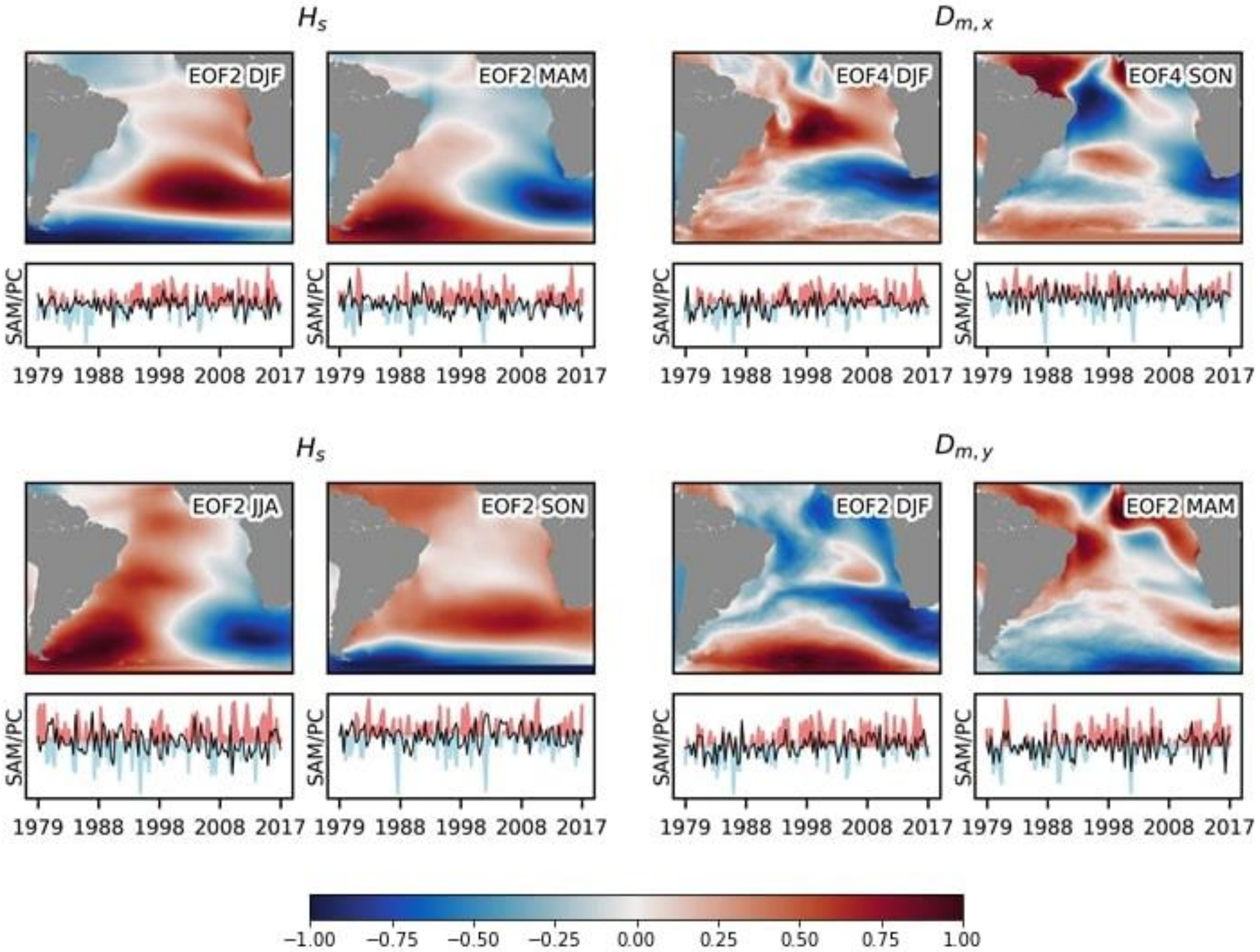

Figure 12 Seasonal composites of selected variability modes of significant wave height (left) and zonal and meridional wave components of wave direction (right). The principal component of the corresponding variability mode is plotted under its respective correlation map, in front of Southern Annular Mode Index, which is plotted as anomaly plot. DJF stands for December, January, February (austral summer), MAM for March, April, May (austral autumn), JJA for June, July, August (austral winter) and SON for September, October, November (austral spring).

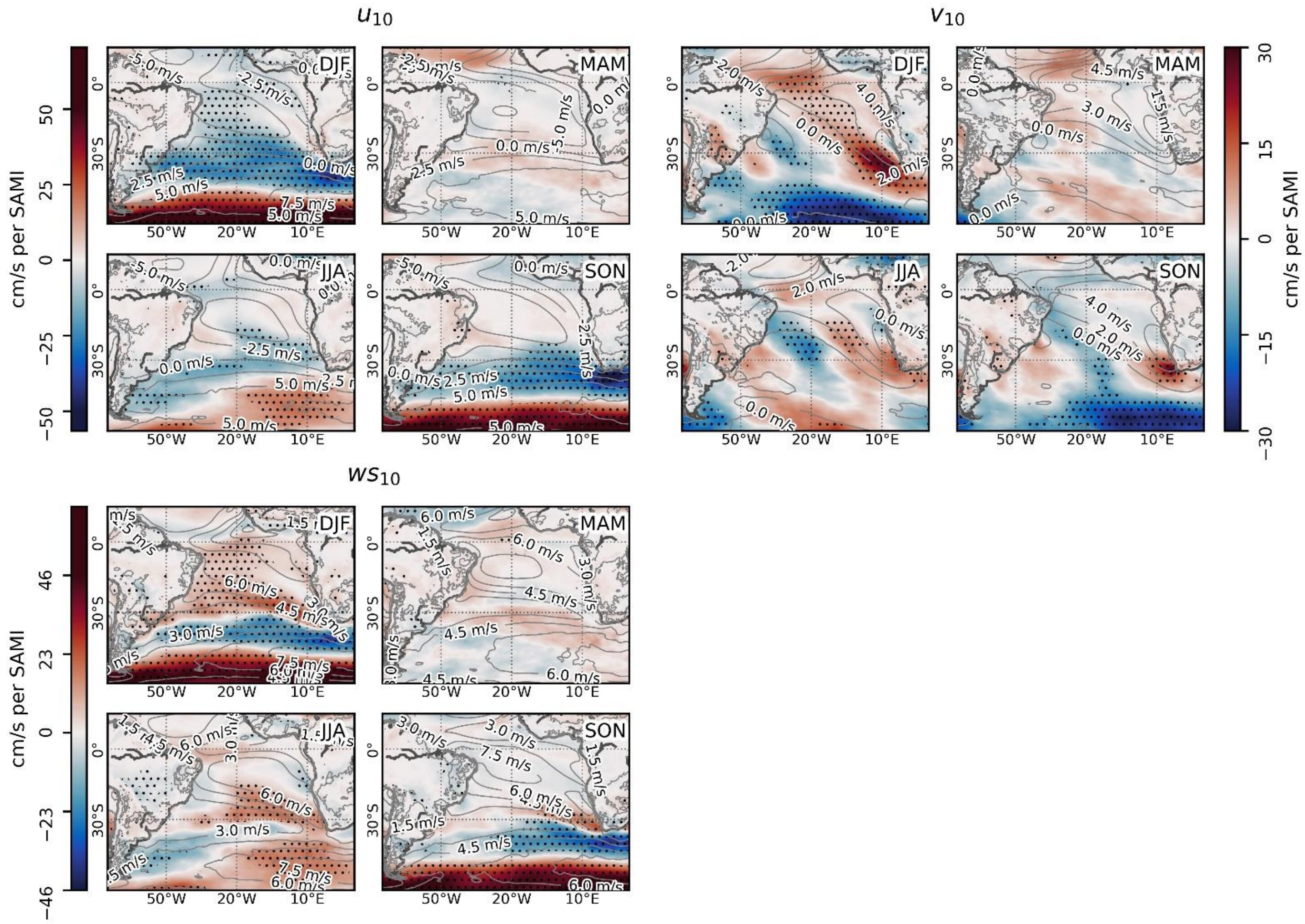

Figure 13 Seasonal composites of zonal and meridional components of 10 m wind (u_{10} and v_{10}, respectively) and wind speed (WS_{10}) regressed against Southern Annular Mode Index. Climatologies are plotted in grey contour levels, and significant positive and negative correlations at 90% confidence level ($p<0.10$) are hatched with black dots. DJF stands for December, January, February (austral summer), MAM for March, April, May (austral autumn), JJA for June, July, August (austral winter) and SON for September, October, November (austral spring).

4 Combined effects of ENSO and SAM

In Section 3, the main effects of SAM, ENSO and PDO upon surface ocean waves analysed over forty years of data are presented. To analyse the combined effects of SAM and ENSO, wave and wind data were subsetted by grouping ENSO and SAMI periods as described in Table 5. For wave parameters, seasonal anomalies were calculated for each group by subtracting the 40-year seasonal average from the actual average of the group. After that, anomalies were mapped. PDO was left out of this analysis because, if included, forty years of data would not be sufficient for obtaining subsets with significant sample size.

Table 5 Description of the subsets used for the calculation of anomalies. Sample size is the number of months included in each subset used for the anomaly calculation

Group	Condition	Sample size (months)			
		DJF	MAM	JJA	SON
El Niño	ONI > 0.5	41	26	24	36
La Niña	ONI < 0.5	41	23	21	35
Positive SAM	SAMI ≥ 1	50	42	44	42
Negative SAM	SAMI ≤ -1	29	24	28	30
El Niño ∩ Positive SAM	ONI > 0.5 ^ SAMI > 1	16	8	10	11
El Niño ∩ Negative SAM	ONI < 0.5 ^ SAMI < -1	11	4	3	12
La Niña ∩ Positive SAM	ONI > 0.5 ^ SAMI > 1	22	6	7	14
La Niña ∩ Negative SAM	ONI < 0.5 ^ SAMI < -1	10	2	7	8

Our focus in this section is to discuss the conditions regarding to different combinations of ENSO and SAM phases. To support this analysis, ENSO and SAM phases were explored individually to support the evaluation of how these oscillations interact.

Recent studies have highlighted the negative correlation between ENSO and SAM, especially during austral spring and summer (Cai et al., 2011; Carvalho et al., 2005; Dätwyler et al., 2020). This finding is also observed here regarding surface ocean waves, with El Niño and negative SAM mostly reinforcing each other's effects and La Niña and positive SAM mostly negating each other's impacts.

Figures 14 and 15 display stronger H_s and T_m anomalies in mid- to high latitudes in the *El Niño ∩ Negative SAM* group. This group also presented intensification of westerly wind anomalies, as one can observe at the composites of wind speed anomalies (Fig. 16). The wave and wind anomalies at south-east SAO are likely to reflect the extratropical dynamics of subtropical jet streams, as they are strengthened by both El Niño and the negative phase of SAM, reinforcing each other's impact. This has the potential of creating waves that propagate to lower latitudes along west African Coast, driving larger waves for south-east SAO.

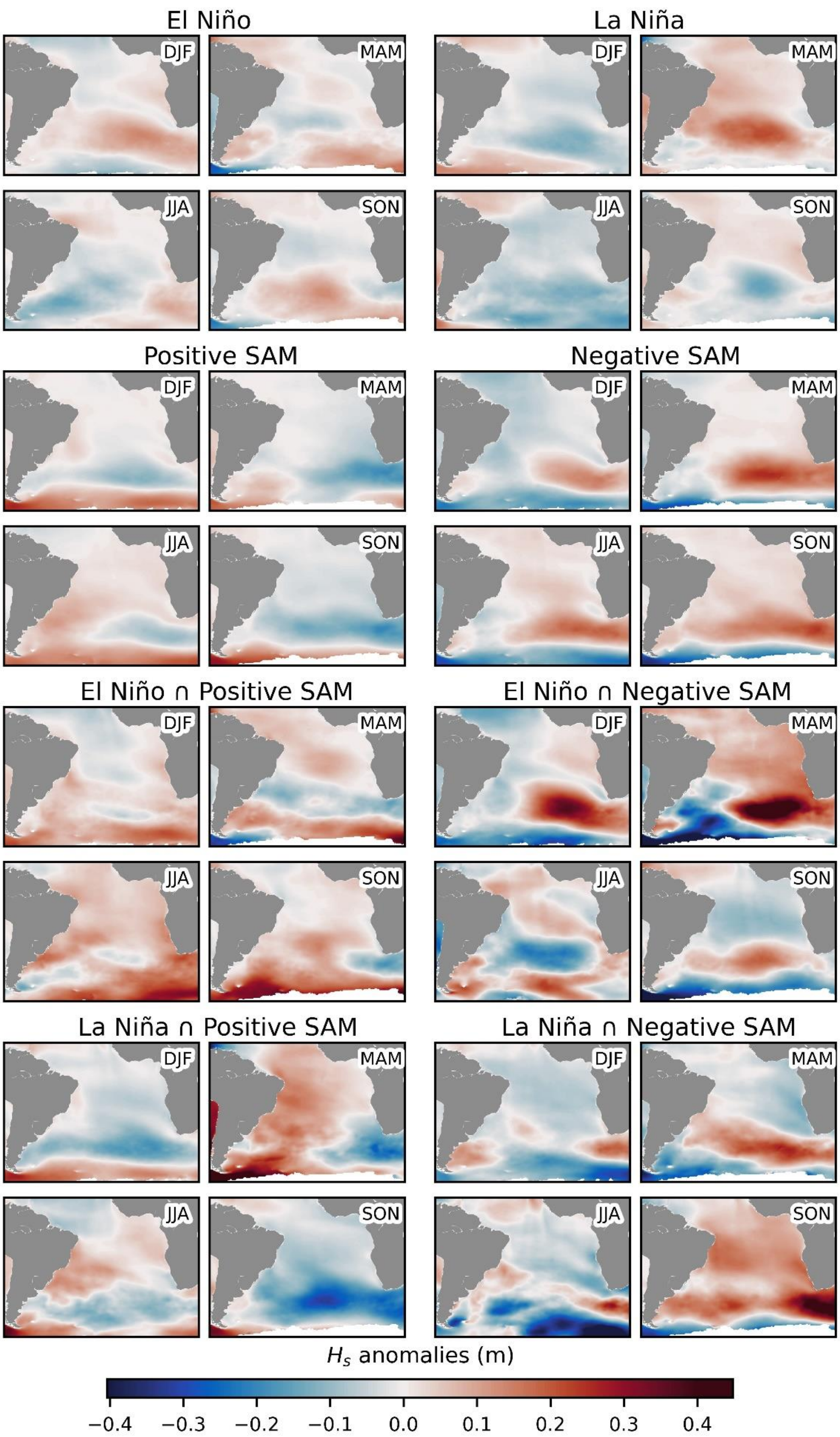

Figure 14 Seasonal significant wave height (H_s) anomalies for El Niño, La Niña, Positive SAM, Negative SAM, and the combination of ENSO and SAM phases.

Both *La Niña* and *Negative SAM* groups display positive H_s, T_m, and WS_{10} anomalies at the south of Africa, especially in austral autumn and spring. In the *La Niña* ∩ *Negative SAM* group, these positive anomalies are intensified. On the other hand, in the *La Niña* ∩ *Positive SAM* group, these anomalies are supressed or have their signal changed to negative. This is likely because positive SAM leads to negative anomalies in the region, and compared to ENSO, SAM is a more significant agent of climate variability for high latitudes. These patterns are also observed in wind speed anomaly composites (Figure 16).

During positive phases of SAM, the upper-level polar jet stream is strengthened, intensifying high latitude easterlies (Thompson and Wallace, 2000). This potentially influences the positive H_s anomalies of up to 0.30 m in high latitudes and in western SAO. The *La Niña* group also presented positive H_s anomalies in high latitudes, especially in summer. In the group *La Niña* ∩ *Positive SAM,* these positive anomalies are enhanced and reach up to 0.45 m (Fig. 14). The *El Niño* group presented weak positive H_s and T_m anomalies in south-east SAO from austral autumn to austral spring. In the *El Niño* ∩ *Positive SAM* group, these anomalies are stronger when compared to the *El Niño* group.

Regarding T_m anomalies (Fig. 15), autumn and winter strong positive anomalies in low latitudes in the *El Niño* ∩ *Positive SAM* group stand out. The timing of these anomalies is interesting, as the literature declares late austral spring as the most active season regarding SAM modulation of trade winds and height of tropopause over mid- to high latitudes (Carvalho et al., 2005; Limpasuvan and Hartmann, 2000; Thompson and Wallace, 2000), and ENSO usually peaks in austral summer (Chen and Jin, 2020). However, as already mentioned, these anomalies might reflect the strengthening of subtropical jet stream during both El Niño and negative SAM events. During winter, the subtropical jet stream displaces northwards, and when El Niño and negative SAM are coupled, these storm-related-ocean-waves are able to propagate even further north.

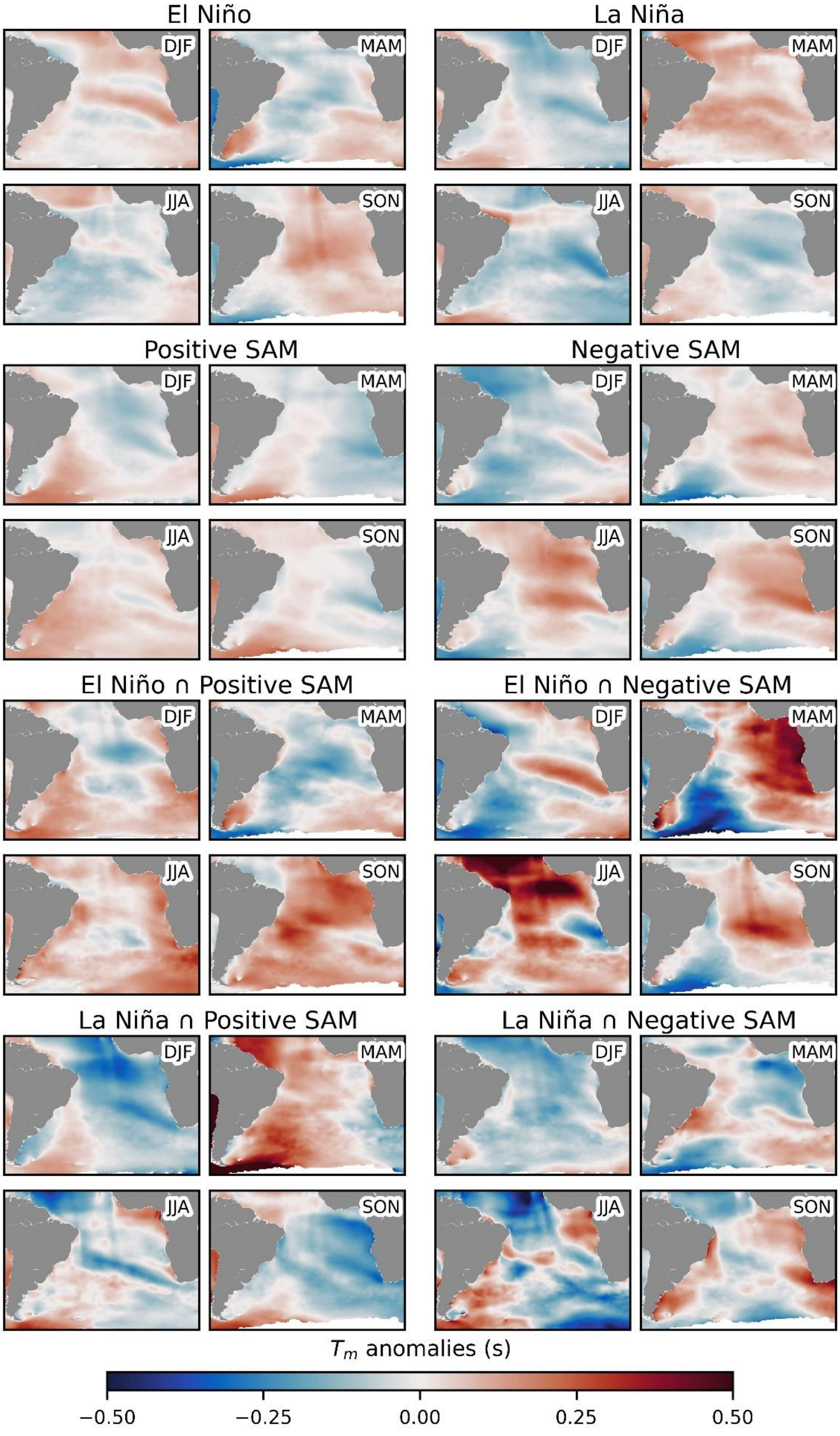

470

Figure 15 Seasonal mean wave period (T_m) anomalies for El Niño, La Niña, Positive SAM, Negative SAM (top) and 471
the combination of ENSO and SAM phases (bottom). 472

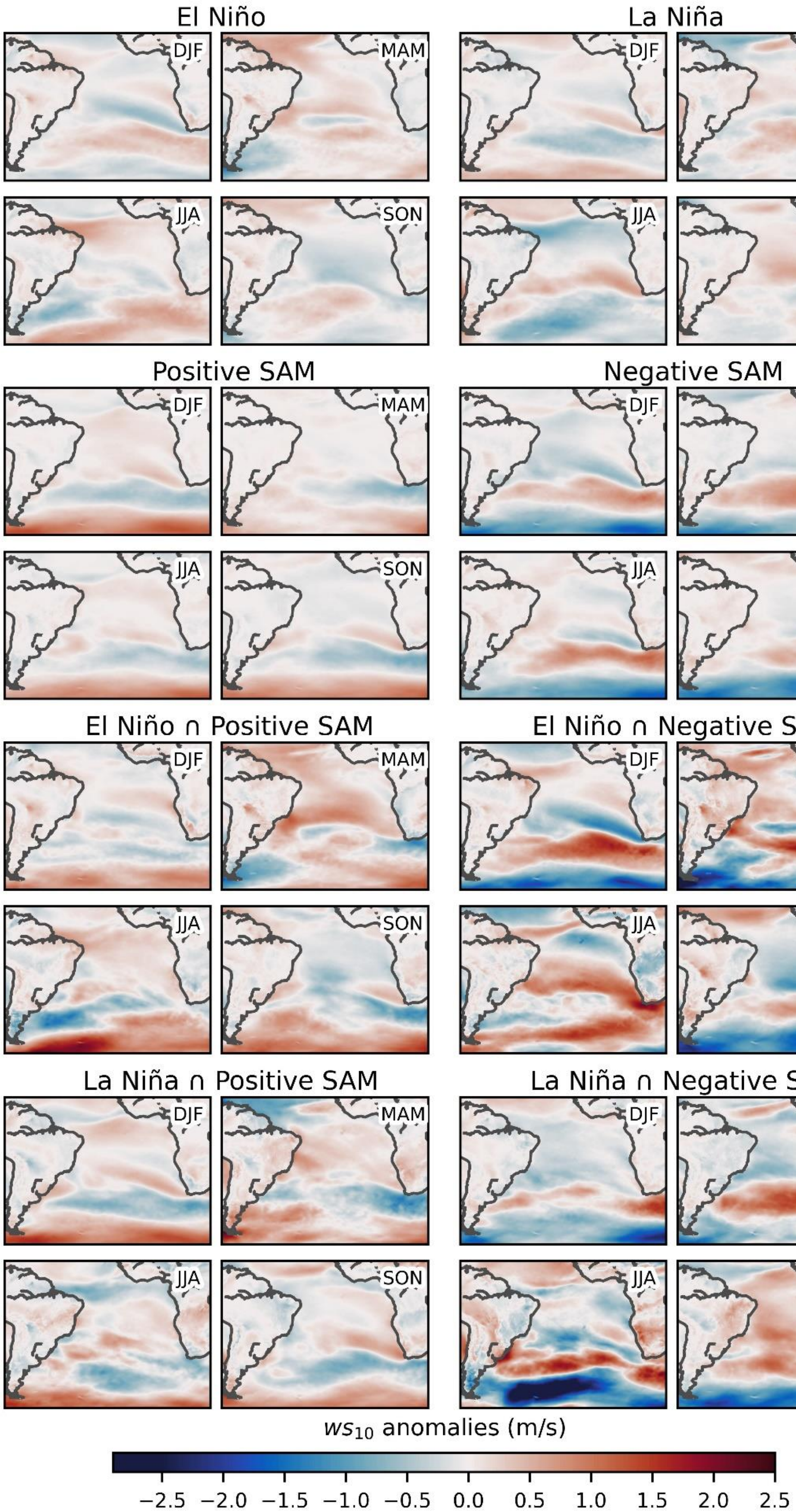

Figure 16 Seasonal wind speed (*WS_{10}*) anomalies for El Niño, La Niña, Positive SAM, Negative SAM (top) and the combination of ENSO and SAM phases (bottom).

4 Conclusions

Our findings and conclusions are summarized as follows: observed climate oscillations modify the SAO wave climate systematically. La Niña events promote larger waves with a more north-westerly component in the northern portion of SAO, suggesting a major entrance of the North Atlantic swell in the region. El Niño events contribute to larger and more south-easterly waves in the eastern SAO. This happens due to the association of this event to mid-latitudes cyclones, a synoptic type responsible for larger waves. Also, El Niño favours wind seas in low latitudes. A positive SAM increases both H_s and T_m in the southernmost SAO and along the Brazilian coast, whereas decreasing these parameters above parallel 50°S. A negative SAM has the opposite effect. A negative PDO increases both H_s and T_m in SAO and changes directional components similarly to a negative ENSO. Positive PDO exerts opposite effects.

Variability modes returned by the EOF analysis represented ocean conditions associated to climate oscillations. Interestingly, the second variability mode of both summer H_s and $D_{m,y}$ is significantly associated to all oscillations here analysed. SAM is the oscillation that most influences wave climate, with at least one among four leading modes of variability of wave parameters in each season being associated to SAMI. ENSO and PDO exert their influence mostly in spring and summer.

It is not feasible to establish a concrete wave state pattern for each of these oscillation phases once they mutually affect each other. However, we can understand what to expect regarding wave parameters in each of these phases when we analyse the entire picture. The effects of ENSO–SAM coupling are a mixture of SAM influence in mid- to high latitudes and ENSO influence in low to mid-latitudes. The anomalies are stronger when ENSO and SAM phases are occurring simultaneously. For example, SAM H_s anomalies at mid- to high latitudes may be strengthened or mitigated depending on ENSO phase. Also, depending on which SAM phase is on, La Niña events prompt either positive H_s and T_p anomalies or negative ones at the south of Africa.

These results of seasonally and spatially variable oscillation effects over wave climate can potentially provide some insight into estimating future wave scenarios in response to changing frequency and magnitude of climate oscillations. Wave driven currents are the primary mode of sediment transport within the coastal zone; thus, understanding the wave climate and acknowledging the influence of climate oscillations over it helps us implement structures for coastal protection, leaving us better prepared to future coastal changes. Moreover, this knowledge can also be used for navigation purposes and as foundation when evaluating potential areas for offshore wave and wind energy exploitation.

References

Allan, J.C., Komar, P.D., 2006. Climate Controls on US West Coast Erosion Processes. J. Coast. Res. 22, 511–529. https://doi.org/10.2112/03-0108.1

Allan, J.C., Komar, P.D., 2000. Are Ocean Wave Heights Increasing in the Eastern North Pacific? EOS Trans. Am. Geophys. Union 81, 561–567.

Angiulli, F., Pizzuti, C., 2002. Fast outlier detection in high dimensional spaces, in: European Conference on Principles of Data Mining and Knowledge Discovery. Springer, Helsinki, pp. 15–27.

Aragão, J.O.R., 1998. Impact dans le nordeste du Brésil de l'ENSO et du Dipôle de l'Atlantique. Bull. l'Institut Français d'Etudes Andin. 27, 839–844.

Aragão, J.O.R., 1986. A general circulation model investigation of the atmospheric response to El Niño. PhD thesis, University of Miami, Miami.

Bhaskaran, B., Mullan, A.B., 2003. El Niño-related variations in the southern Pacific atmospheric circulation: Model versus observations. Clim. Dyn. 20, 229–239. https://doi.org/10.1007/s00382-002-0276-2

Bjerknes, J., 1966. A possible response of the atmospheric Hadley circulation to equatorial anomalies of ocean temperature. Tellus 18, 820–829. https://doi.org/10.3402/tellusa.v18i4.9712

Cai, W., Sullivan, A., Cowan, T., 2011. Interactions of ENSO, the IOD, and the SAM in CMIP3 models. J. Clim. 24, 1688–1704. https://doi.org/10.1175/2010JCLI3744.1

Carvalho, L.M. V., Jones, C., Ambrizzi, T., 2005. Opposite Phases of the Antarctic Oscillation and Relationships with Intraseasonal to Interannual Activity in the Tropics during the Austral Summer. J. Clim. 18, 702–718.

Chen, H.C., Jin, F.F., 2020. Fundamental behavior of ENSO phase locking. J. Clim. 33, 1953–1968. https://doi.org/10.1175/JCLI-D-19-0264.1

Dalinghaus, C., 2016. Análise da estabilidade da forma em planta e perfil nas praias da Barra da Lagoa, Moçambique e Ingleses, Florianópolis - SC: Aplicações em análise de perigos costeiros. Master's thesis, Universidade Federal de Santa Catarina, Florianópolis.

Dätwyler, C., Grosjean, M., Steiger, N.J., Neukom, R., 2020. Teleconnections and relationship between the El Niño-Southern Oscillation (ENSO) and the Southern Annular Mode (SAM) in reconstructions and models over the past millennium. Clim. Past 16, 743–756. https://doi.org/10.5194/cp-16-743-2020

Dawson, A., 2016. eofs: A Library for EOF Analysis of Meteorological, Oceanographic, and Climate Data. J. Open Res. Softw. 4, 4–7. https://doi.org/10.5334/jors.122

Dodet, G., Bertin, X., Taborda, R., 2010. Wave climate variability in the North-East Atlantic Ocean over the last six decades. Ocean Model. 31, 120–131. https://doi.org/10.1016/j.ocemod.2009.10.010

GEBCO Compilation Group, 2020. GEBCO 2020 Grid. https://doi.org/10.5285/a29c5465-b138-234de053-6c86abc040b9

Gershunov, A., Barnett, T.P., 1998. Interdecadal Modulation of ENSO Teleconnections. Bull. Am. Meteorol. Soc. 79, 2715–2725.

Gulev, S.K., Grigorieva, V., 2006. Variability of the winter wind waves and swell in the North Atlantic and North Pacific as revealed by the voluntary observing ship data. J. Clim. 19, 5667–5685. https://doi.org/10.1175/JCLI3936.1

Hardiman, S.C., Dunstone, N.J., Scaife, A.A., Smith, D.M., Ineson, S., Lim, J., Fereday, D., 2019. The Impact of Strong El Niño and La Niña Events on the North Atlantic. Geophys. Res. Lett. 46, 2874–2883. https://doi.org/10.1029/2018GL081776

Held, I.M., Lyons, S.W., Nigam, S., 1989. Transients and the extratropical response to El Nino. J. Atmos. Sci. https://doi.org/10.1175/1520-0469(1989)046<0163:TATERT>2.0.CO;2

Hemer, M.A., Church, J.A., Hunter, J.R., 2010. Variability and trends in the directional wave climate of the Southern Hemisphere. Int. J. Climatol. 30, 475–491. https://doi.org/10.1002/joc.1900

Hemer, M.A., Simmonds, I., Keay, K., 2008. A classification of wave generation characteristics during large wave events on the Southern Australian margin. Cont. Shelf Res. 28, 634–652. https://doi.org/10.1016/j.csr.2007.12.004

Hersbach, H., Bell, B., Berrisford, P., Hirahara, S., Horányi, A., Muñoz-Sabater, J., Nicolas, J., Peubey, C., Radu, R., Schepers, D., Simmons, A., Soci, C., Abdalla, S., Abellan, X., Balsamo, G., Bechtold, P., Biavati, G., Bidlot, J., Bonavita, M., De Chiara, G., Dahlgren, P., Dee, D., Diamantakis, M., Dragani, R., Flemming, J., Forbes, R., Fuentes, M., Geer, A., Haimberger, L., Healy, S., Hogan, R.J., Hólm, E., Janisková, M., Keeley, S., Laloyaux, P., Lopez, P., Lupu, C., Radnoti, G., de Rosnay, P., Rozum, I., Vamborg, F., Villaume, S., Thépaut, J.N., 2020. The ERA5 global reanalysis. Q. J. R. Meteorol. Soc. 1–51. https://doi.org/10.1002/qj.3803

Hunter, J.D., 2007. Matplotlib: A 2D graphics environment. Comput. Sci. Eng. 9, 99–104. https://doi.org/10.1109/MCSE.2007.55

Iza, M., Calvo, N., Manzini, E., 2016. The stratospheric pathway of La Niña. J. Clim. 29, 8899–8914. https://doi.org/10.1175/JCLI-D-16-0230.1

Karoly, D.J., 1989. Southern Hemisphere Circulation Features Associated with El Niño-Southern Oscillation Events. J. Clim. https://doi.org/10.1175/1520-0442(1989)002<1239:shcfaw>2.0.co;2

Kousky, V.E., Kagano, M.T., Cavalcanti, I.F.A., 1984. A review of the Southern Oscillation: oceanic-atmospheric circulation changes and related rainfall anomalies. Tellus A 36, 490–504. https://doi.org/10.1111/j.1600-0870.1984.tb00264.x

Laing, A.K., 2000. New Zealand wave climate from satellite observations. New Zeal. J. Mar. Freshw. Res. 34, 727–744. https://doi.org/10.1080/00288330.2000.9516973

Limpasuvan, V., Hartmann, D.L., 2000. Wave-Maintained Annular Modes of Climate Variability. J. Clim. 13, 4414–4429. https://doi.org/10.1175/2010JCLI3458.1

Mantua, N.J., Hare, S.R., 2002. The pacific decadal oscillation. J. Oceanogr. 58, 35–44.

Marshall, A.G., Hemer, M.A., Hendon, H.H., McInnes, K.L., 2018. Southern annular mode impacts on global ocean surface waves. Ocean Model. 129, 58–74. https://doi.org/10.1016/j.ocemod.2018.07.007

Menéndez, M., Méndez, F.J., Losada, I.J., Graham, N.E., 2008. Variability of extreme wave heights in the northeast Pacific Ocean based on buoy measurements. Geophys. Res. Lett. 35, 1–6. https://doi.org/10.1029/2008GL035394

Moron, V., Gouirand, I., 2003. Seasonal modulation of the El Niño-southern oscillation relationship with sea level pressure anomalies over the North Atlantic in October-March 1873-1996. Int. J. Climatol. 23, 143–155. https://doi.org/10.1002/joc.868

Oliveira, B.A., Sobral, F., Fetter, A., 2017. Variabilidade do clima de ondas de Santa Catarina utilizando o modelo Wavewatch III Santa Catarina wave climate variability using Wavewatch III model. Universidade Federal de Santa Catarina.

Pereira, N.E. da S., Klumb-Oliveira, L.A., 2015. Analysis of the influence of ENSO phenomena on wave climate on the central coastal zone of Rio de Janeiro (Brazil). J. Integr. Coast. Zo. Manag. 15, 353–370. https://doi.org/10.5894/rgci570

Pezza, A.B., Simmonds, I., Renwick, J.A., 2007. Southern Hemisphere cyclones and anticyclones: Recent trends and links with decadal variability in the Pacific Ocean. Int. J. Climatol. 27, 1403–1419. https://doi.org/10.1002/joc

Phinn, S.R., Hastings, P.A., 1995. Southern Oscillation influences on the Gold Coast’s summer wave climate. J. Coast. Res. 11, 946–958.

Ramaswamy, S., Rastogi, R., Shim, K., 2000. Efficient algorithms for mining outliers from large data sets. ACM Sigmod Rec. 29, 427–438.

Ranasinghe, R., McLoughlin, R., Short, A., Symonds, G., 2004. The Southern Oscillation Index, wave climate, and beach rotation. Mar. Geol. 204, 273–287. https://doi.org/10.1016/S0025-3227(04)00002-7

Reguero, B.G., Méndez, F.J., Losada, I.J., 2013. Variability of multivariate wave climate in Latin America and the Caribbean. Glob. Planet. Change 100, 70–84.

https://doi.org/10.1016/j.gloplacha.2012.09.005

Ruggiero, P., Komar, P.D., Allan, J.C., 2010. Increasing wave heights and extreme value projections: The wave climate of the U.S. Pacific Northwest. Coast. Eng. 57, 539–552. https://doi.org/10.1016/j.coastaleng.2009.12.005

Semedo, A., Sušelj, K., Rutgersson, A., 2009. Variability of Wind Sea and Swell Waves in the North Atlantic Based on ERA-40 Re-analysis. Proc. 8th Eur. Wave Tidal Energy Conf. 119–129.

Souza, E.D., Ambrizzi, T., 2002. ENSO impacts on the South American rainfall during 1980s: Hadley and Walker circulation. Atmósfera 15, 105–120.

Thompson, D.W.J., Wallace, J.M., 2000. Annular modes in the extratropical circulation. Part I: Month-to-month variability. J. Clim. 13, 1000–1016. https://doi.org/10.1175/1520-0442(2000)013<1000:AMITEC>2.0.CO;2

Woolf, D.K., Challenor, P.G., Cotton, P.D., 2002. Variability and predictability of the North Atlantic wave climate. J. Geophys. Res. C Ocean. 107, 1–14. https://doi.org/10.1029/2001jc001124

Young, I.R., 1999. Seasonal variability of the global ocean wind and wave climate. Int. J. Climatol. 19, 931–950. https://doi.org/10.1002/(SICI)1097-0088(199907)19:9<931::AID-JOC412>3.0.CO;2-O

Zhang, W., Mei, X., Geng, X., Turner, A.G., Jin, F.F., 2019. A nonstationary ENSO-NAO relationship due to AMO modulation. J. Clim. 32, 33–43. https://doi.org/10.1175/JCLI-D-18-0365.1

Zhang, Y., Wallace, J.M., Battisti, D.S., 1997. ENSO-like interdecadal variability: 1900-93. J. Clim. 10, 1004–1020. https://doi.org/10.1175/1520-0442(1997)010<1004:eliv>2.0.co;2

Zhao, Y., Nasrullah, Z., Li, Z., 2019. PyOD: A python toolbox for scalable outlier detection. J. Mach. Learn. Res. 20, 1–7.

Zimmermann, D.F.R., 2017. Subtropical jet climatology over south america. Master's thesis, University of São Paulo, São Paulo.